International Journal of Biological Macromolecules 328 (2025) 147640

Contents lists available at ScienceDirect

International Journal of Biological Macromolecules

journal homepage: www.elsevier.com/locate/ijbiomac

Xanthan gum-based Magnosorbent: A selective, rapid, and high-capacity adsorbent for pH-tolerant methylene blue removal from complex pollutant systems

Ayşegül Ülkü Metin [a,*], Nesrin Horzum [b], Abdurrahman Dağcı [a], Ahmet Tarık Savaş [a]

[a] Department of Chemistry, Faculty of Engineering and Natural Sciences, Kırıkkale University, Yahşihan, 71450, Kırıkkale, Türkiye
[b] Department of Engineering Sciences, Faculty of Engineering and Architecture, and Polymeric Nanocomposites Applications Laboratory (PNCA Lab), İzmir Katip Çelebi University, 35620, İzmir, Türkiye

ARTICLE INFO

Keywords:
Dual functionalization
Eco-friendly remediation
Magnetic nanocomposite
pH-tolerant adsorption
Rapid kinetics
Selective adsorption
Xanthan gum

ABSTRACT

Efficient and sustainable removal of dyes from wastewater remains a critical challenge in environmental remediation. ***Magnosorbent,*** a magnetically retrievable, dual-functionalized biopolymer-based nanocomposite, was designed by integrating xanthan gum (XG), a natural and biocompatible polysaccharide, with poly (3-sulfopropyl methacrylate) (PSPMA) which is also recognized for its biocompatibility, to enable efficient, selective, and sustainable removal of methylene blue (MB) from complex pollutant systems. This design enables a synergistic combination of magnetic recoverability, pH-resilient adsorption, and selective dye affinity. Comprehensive characterization confirmed the structural, chemical, and magnetic properties of the nanocomposite. The material exhibited an amorphous nature, with a saturation magnetization of 38.075 emu/g and a BET surface area of 46.68 m^2/g, supporting magnetic separability and high surface accessibility. The adsorption process followed the Langmuir isotherm model, achieving a maximum capacity of 235 mg/g, and demonstrated spontaneity and exothermic behavior. ***Magnosorbent*** showed remarkable stability and efficiency across a broad pH range (2−12), retaining high adsorption efficiency. The rapid kinetics (≥80 % removal within 5 min) and ease of magnetic recovery underscore its practical applicability. High adsorption performance for MB was maintained even in complex multi-pollutant mixtures, retaining over 72 % removal efficiency despite competition from interfering cations, heavy metal ions, endocrine-disrupting compounds, dye mixtures, and surface-active agents. The nanocomposite maintained robust performance over multiple regeneration cycles and batch-to-batch reproducibility, highlighting its reusability. These results position *Magnosorbent* as a scalable, eco-friendly solution for industrial wastewater treatment, with potential extensions to other environmental pollutants.

1. Introduction

The rapid development of industrialization has dramatically intensified water pollution, introducing harmful pollutants such as microplastics, dyes, and pharmaceutical compounds into aquatic ecosystems. These pollutants not only disrupt marine life but also pose serious risks to human health, as they can enter the food chain, gradually accumulate in the body, and potentially cause allergic reactions, genetic mutations, or even cancer [1,2]. The increasing prevalence of such pollutants highlights the urgent need for effective strategies to protect water quality and safeguard public health. Common methods for pollutant removal include chemical oxidation, coagulation-flocculation, membrane filtration, and biodegradation. While these approaches are widely utilized, they often encounter limitations such as high energy consumption, operational complexity, and the generation of secondary waste, which can compromise their sustainability and efficiency. Among these methods, adsorption has emerged as a highly efficient and environmentally friendly alternative. Its advantages include low energy requirements, ease of scalability, and broad applicability in the removal of undesired pollutants [3]. A variety of adsorbent materials-ranging from carbon-based compounds, metal oxides to polymer-based nanoparticles, films, and nanofibers-have demonstrated exceptional potential in mitigating water pollution and ensuring environmental safety [4–7]. Many traditional adsorbents exhibit limited selectivity, slow kinetics, narrow operating pH ranges, or lack reusability, restricting their practical implementation in industrial settings.

* Corresponding author.
E-mail address: aumetin@gmail.com (A.Ü. Metin).

https://doi.org/10.1016/j.ijbiomac.2025.147640
Received 30 May 2025; Received in revised form 2 September 2025; Accepted 10 September 2025
Available online 11 September 2025

Beyond the limitations of the traditional adsorbents, the compositional diversity, toxicity, and persistence of pollutants in water necessitate the use of adsorbents with specific functionalities that offer high selectivity toward targeted pollutants. One particularly challenging category of such pollutants is cationic dyes, such as methylene blue (MB), which interact with negatively charged cell membranes, posing significant environmental and health concerns associated with colored wastewater [8–11]. This interaction facilitates the penetration of dyes into cells and their accumulation in the cytoplasm, thereby exacerbating their detrimental impact on aquatic ecosystems in rivers and lakes. MB, a stable organic molecule, is widely used in dyeing silk, wool, and cotton textiles, making it a prominent component of colored wastewater [12,13]. Due to its complex and stable aromatic structure, MB is resistant to natural degradation. Furthermore, it exhibits high toxicity and is linked to sensitization, mutagenicity, and carcinogenic effects. Consequently, the International Agency for Research on Cancer classifies MB as a Group 3 carcinogen [14,15]. To address the challenge of MB removal, various materials, including carbon-based materials [16–20], metal oxides [21–23], and polymer-based materials [24–29] have been extensively developed. Graphene oxide (GO), a well-known carbon-based material with abundant oxygen-containing functional groups, is widely used for the adsorption of cationic dyes [30]. Molla et al. demonstrated that GO selectively adsorbs MB from a binary MB/methyl orange (MO) mixture [31]. In contrast, Molavi et al. noted that nanodiamond, which generally possesses many oxygen-containing functional groups on its outer surface, adsorbed MO instead of MB from the MB/MO mixture due to the scarcity of carboxyl groups [32]. Metal-based materials, particularly metal oxides, have also been employed for the dye removal. For instance, Zahra et al. investigated the adsorption of MB using vanadium phosphorus oxide embedded in a TiO_2 matrix [33]. Among these materials, magnetic oxides are the most commonly utilized due to their unique properties. Magnetic particles, often modified with polymers or other materials, serve as cores for the formation of magnetic nanocomposites, which offer higher efficiency, ease of separation, surface tunability, and a more sustainable alternative to traditional adsorbents [34]. Notable examples include magnetic activated carbon [35], Fe_3O_4/graphene [36], and magnetic multi-walled carbon nanotubes [37]. Recent advancements have focused on incorporating polymers, biomaterials, and functional nanoparticles into magnetic nanocomposites to increase the density and diversity of functional groups, thereby enhancing adsorption capacity, selectivity toward specific dyes, and stability under varying environmental conditions [38]. These modifications not only improve surface attachment but also enable rapid separation and recovery post-adsorption [39]. For example, Xie et al. synthesized Fe_3O_4/β-cyclodextrin-based polymer composites for MB removal, demonstrating a pH-dependent adsorbent with optimal performance around neutral pH (~7) [38]. Similarly, Sorajini et al. developed a PPy-Fe_3O_4-SW nanocomposite to remove MB from synthetic solutions, with the highest adsorption capacity achieved at alkaline conditions (optimal at pH 10) [39]. Ma et al. prepared magnetic iron-manganese oxides-acrylic polymer composites for MB adsorption, though regeneration performance and adsorption/desorption cycles were not explored, limiting insights into the reusability [14]. In our previous study, we utilized a polymethacrylic acid-magnetic cellulose nanocomposite as an adsorbent for MB removal [40]. Like many studies in this field, these works primarily focused on MB adsorption from synthetic solutions and did not evaluate performance in multi-pollutant or real wastewater systems, limiting understanding of their practical applicability. Hence, there remains a need for adsorbents that combine fast kinetics, broad pH applicability, high adsorption capacity, and efficient regeneration—especially for treating complex, multi-dye wastewater systems.

Unlike previous systems, the nanocomposite developed in this study integrates a natural biopolymer backbone with sulfonic acid-rich functionalization and magnetic properties, enabling rapid and selective dye capture across diverse conditions. We developed a polymeric and magnetic nanocomposite based on xanthan gum impregnated with poly (3-sulphopropyl methacrylate) (mXG/PSPMA). The combination of XG and PSPMA exhibits enhanced responsiveness to environmental stimuli, with sulfonic acid groups of PSPMA facilitating adaptability, while gel-forming nature of XG contributes to the durability and smart functionality of the material. *Magnosorbent* was prepared via a combination of sequential physical cross-linking and graft *co*-polymerization. The physicochemical properties of *magnosorbent* were characterized using Fourier Transform Infrared Spectroscopy (FTIR), Scanning Electron Microscopy (SEM) with Energy Dispersive Spectroscopy (EDS), Transmission Electron Microscopy (TEM), Vibration Sample Magnetometer (VSM), X-ray Diffraction (XRD), and Brunauer–Emmett–Teller (BET).

This study aims to develop an advanced magnetically retrievable, dual-functionalized mXG/PSPMA nanocomposite for the rapid and selective MB remval from complex aqueous environments, including interfering cations, heavy metal ions, endocrine-disrupting compounds, dye mixtures, surface active agents, and real water samples. Comprehensive investigations into the adsorption kinetics, isotherms, and thermodynamic aspects, and mechanism were conducted. *Magnosorbent* exhibited several significant advantages: (1) An oxygen-enriched surface with different functional groups, enhancing adsorption efficiency (98.04 % at 50 mg dosage); (2) Broad applicability across a broad pH range (2–12), ensuring versatility under varying conditions; (3) Rapid adsorption kinetics, achieving ≥80 % MB removal within just 5 min; (4) Despite competitive ions and complex contaminant mixtures, *magnosorbent* retains exceptional selectivity for MB, achieving >72 % removal efficiency in multicomponent systems. Its hierarchical adsorption mechanism, prioritizing electrostatic attraction, π-π stacking, and porous uptake, ensures robust performance; (5) *Magnosorbent* exhibits exceptional regeneration capability, maintaining 65–88 % MB removal efficiency over eight cycles due to its magnetic recoverability and chemical stability. Batch-to-batch reproducibility (<25 % variation in adsorption capacity) and scalable synthesis further highlight its practical viability, with cost-effectiveness enhanced by reusable performance and multi-pollutant targeting.

2. Materials and methods

2.1. Reagents

The reagents used in this study are detailed in the Supplementary Data (Text S1).

2.2. Preparation of mXG/PSPMA nanocomposite

The mXG/PSPMA nanocomposite was synthesized using xanthan gum and 3-sulphopyropyl methacrylate, following modified methods from previous studies [41,42]. The schematic illustration of the synthesis process is shown in Fig. 1. In brief, a homogeneous XG solution (1 % *w/v*, 12.5 mL) was prepared in Fe(III) solution (1.0 M, $FeCl_3{\cdot}6H_2O$) in a water bath at 60 °C. Subsequently, SPMA monomer (1–4 % *w/v*), potassium persulphate (KPS, 0.1 % w/v), and *N*, *N*-methylene bisacrylamide (MBA, 0.15 % w/v) were introduced to the reaction medium, which was stirred continuously for 2 h in a thermostatic water bath at 60 °C. After the polymerization reaction, excess monomer and Fe (III) ions were removed by centrifugation at 5 °C. Next, Fe(II) solution (0.05 M, 15 mL, $FeSO_4{\cdot}7H_2O$) was added to the reaction medium, and the temperature was raised to 70 °C. Following the homogeneous dispersion of Fe(II) ions onto Fe(III)-adsorbed XG/PSPMA for 30 min, a 25 % NH_3 solution was introduced, and the magnetization reaction was allowed to proceed for 2 h. Upon completion of the reaction, the resulting mXG/PSPMA particles were separated from the solution using a magnet and washed sequentially with distilled water and alcohol for at least three cycles. Grafting yield was calculated using following equation, where m_g is the weight of the grafted copolymer and m_c is the weight of the monomer used.

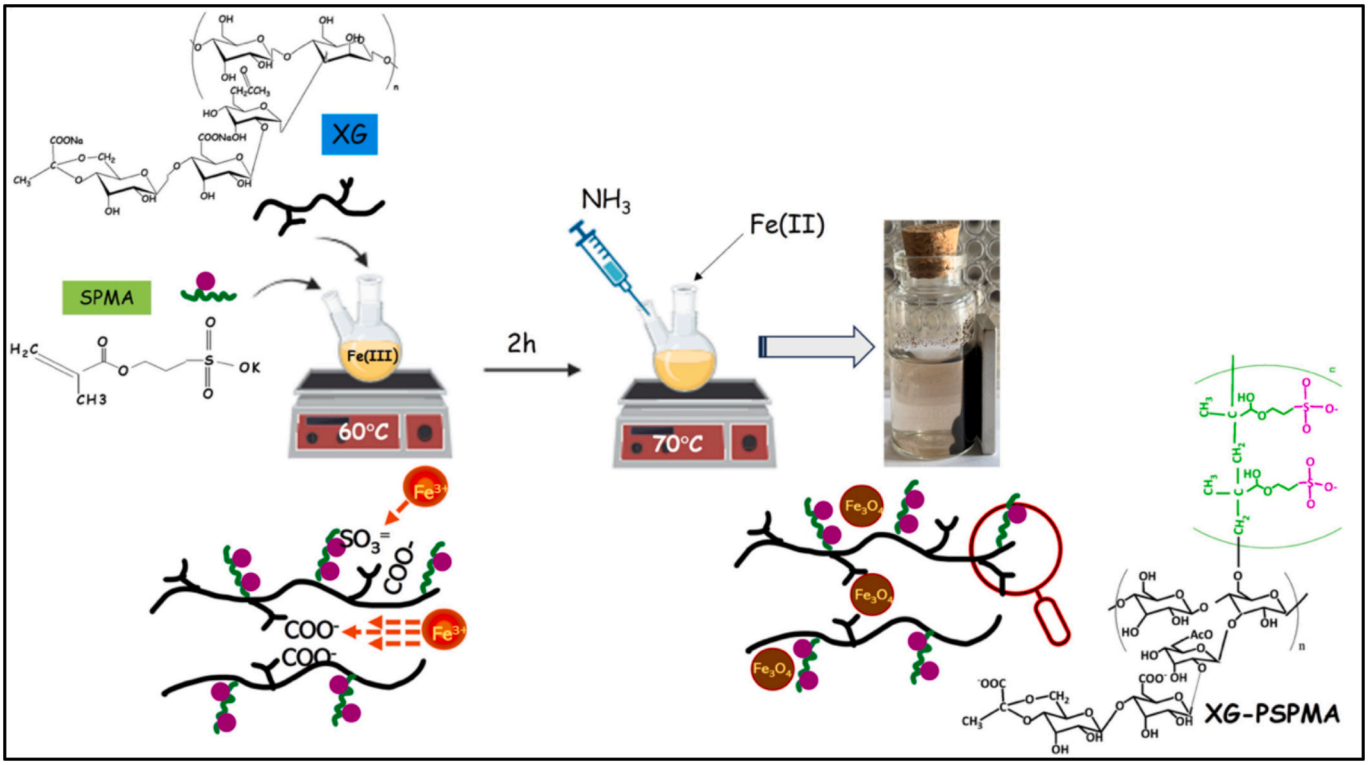

Fig. 1. A schematic illustration for the sequential synthesis and assembly pathway of the mXG/PSPMA.

$$Grafting\ yield\ (\%) = \frac{m_g}{m_c} x100 \quad (1)$$

2.3. Characterization

A comprehensive description of the characterization methods used in this study are provided in the Supplementary Data (Text S2).

2.4. Adsorption study

2.4.1. Efficiency under varying operational scenarios

MB removal experiments in batch systems, were performed in 25 mL solutions, modifying key adsorption parameters including pH, temperature, and the initial MB concentration. The pH of the MB solution was varied from 2 to 12, while the adsorbent dosage was changed from 0.4 to 4 g/L. Following the adsorption process, the mXG/PSPMA was separated using a magnet, and the remaining dye concentration was determined spectrophotometrically at 650 nm.

The equilibrium capacity (q) and the dye removal percentage (R %) were determined using Eqs. (2) and (3), respectively.

$$q\ (mg/g) = \frac{(C_0 - C_e)V}{m} \quad (2)$$

$$R\% = \frac{(C_0 - C_e)}{C_0} x100 \quad (3)$$

Here, C_o and C_e represent the initial and the equilibrium concentrations (mg/L), respectively, m denotes the weight of the mXG/PSPMA (mg), and V refers to volume of the MB solution (mL).

The MB adsorption efficiency of the mXG/PSPMA was also evaluated under varying operational scenarios, including the interfering cations (C+; Na^+, K^+, Ca^{2+}, and NH_4^+), ~~and~~ heavy metal ions (HMIs; Cu^{2+}, Cd^{2+}, Cr^{3+}, Ni^{2+}, Fe^{3+}, Zn^{2+}, Mn^{2+}), dye mixtures (DMix; MG, RB, RB-4, IC, and CR), endocrine-disrupting compounds (EDCs; carbamazepine, ibuprofen, paracetamol), and surface active agents (SAAs; Tween80 and sodium lauryl sulfate (SLS)). Calibration curves for the MB (0.5–4 mg/L) and EDCs (0.002–0.625 mg/mL) are presented in Supplementary Data (Fig. S1). The limits of detection (LOD) and quantification (LOQ) were calculated based on signal-to-noise (S/N) ratios of 3 and 10, respectively. The LOD and LOQ were 0.01380 mg/L and 0.04631 mg/L for MB, and 0.0528 ng/mL and 0.1761 ng/mL for EDCs, respectively.

The competing species were introduced to MB solutions (50 mg/L, pH 7) at environmentally relevant concentrations: C^+ (0–400 mg/L), HMIs (0–10 mg/L), DMix (0–50 mg/L). For EDCs, complete dissolution was achieved at a final pH of 12 (0.04 mg/mL solutions). Tween 80 (1 %, v/v) and SLS (0.1 %, w/v) were used as SAAs in the experiments.

Additionally, the real water samples used in this study were collected as tap water from a residential area in Kırıkkale, Türkiye, on 12 February 2024, and were used without any additional pretreatment to evaluate the practical performance of the nanocomposite under optimal experimental conditions. All experiments were performed in triplicate.

2.4.2. Examination of adsorption kinetics, isotherm characteristics, and thermodynamic aspects

Detailed information on the kinetics, isotherm, and thermodynamic analyses, including experimental procedures and calculation methods, is provided in Supplementary Data (Text S3).

2.4.3. Regeneration, recyclability, and reproducibility study

The reusability of mXG/PSPMA was assessed through multiple adsorption-desorption cycles. Initially, 25 mg of mXG/PSPMA were added to 25 mL of MB solution (50 mg/L) and allowed to adsorb the dye until equilibrium was reached. After adsorption, the MB-loaded mXG/PSPMA were incubated in a 0.1 M NaOH solution for 2 h to desorb the dye. The desorbed particles were then thoroughly rinsed with deionized water until a neutral pH was achieved before the next cycle. This adsorption-desorption process was repeated for a total of 8 cycles. The efficiency of various agents for MB desorption was also evaluated, including citric acid (0.1 M), NaCl (0.5 M), acetic acid (0.1 M), and a mixture of acetic acid (0.1 M) with ethanol (50:50, v/v).

Batch-to-batch reproducibility experiments were conducted using

mXG/PSPMA prepared at different times. The MB removal capacity under optimal conditions was determined, and the reusability of each batch was evaluated over five cycles at maximum capacity.

3. Results and discussion

3.1. Preparation and characterization of mXG/PSPMA

The mXG/PSPMA were synthesized in situ by chemically co-precipitating Fe(III)/Fe(II) ions (molar ratio of ~50/3) in a basic medium and copolymerizing SPMA onto XG. The sulfonic acid groups of PSPMA on the XG chains provide additional active sites, thereby enhancing adsorption capacity. A schematic illustration of the mXG/PSPMA preparation process is shown in Fig. 1. Typically, XG was first homogenized in the Fe(III) solution, and then the APS initiator was added to initiate the graft copolymerization. The possible reaction of the graft copolymer begins with the cleavage of the O—H bond of XG, producing XG macroradicals (XGO•) [43]. XGO• macroradicals react with the SPMA monomer to form free SPMA radicals (RSPMA•), initiating a series of chain growth reactions that ultimately lead to the formation of the graft copolymer and homopolymer (Fig. 2). During this process, electrostatic interactions and ionic crosslinking occurred between Fe(III) ions and the carboxyl groups on XG chains. The success of the graft copolymerization and the effect of SPMA concentration on copolymerization efficiency were evaluated by calculating the percentage of grafting efficiency. Accordingly, the SPMA concentration was changed between 1 %, 2 %, and 4 % *w/v*, the grafting efficiency was calculated as 40 ± 5 %, 110 ± 8 %, and 55 ± 2 %, respectively. FTIR analysis was also used to follow the effect of SPMA concentration (Supplementary Data, Fig. S2). Functional group signals were most pronounced at 2 % SPMA concentration, consistent with the highest grafting efficiency obtained experimentally. Therefore, we proceeded with magnetization studies at this concentration.

The grafting efficiency values increased when the SPMA concentration was raised from 1 % to 2 %, followed by a decrease with further increases in SPMA concentration within the polymerization medium. This initial rise in grafting efficiency is attributed to the enhanced diffusion of SPMA molecules into the XG chains as monomer concentration increases in the reaction mixture. Further increase in SPMA concentration, the termination reaction rates among these macroradicals surpass the rates of combination between SPMA radicals and XG chains, potentially resulting in reduced grafting efficiency. In addition, the viscosity of the reaction medium increases, which restricts the diffusion of SPMA radicals into the XG chains and may further decrease

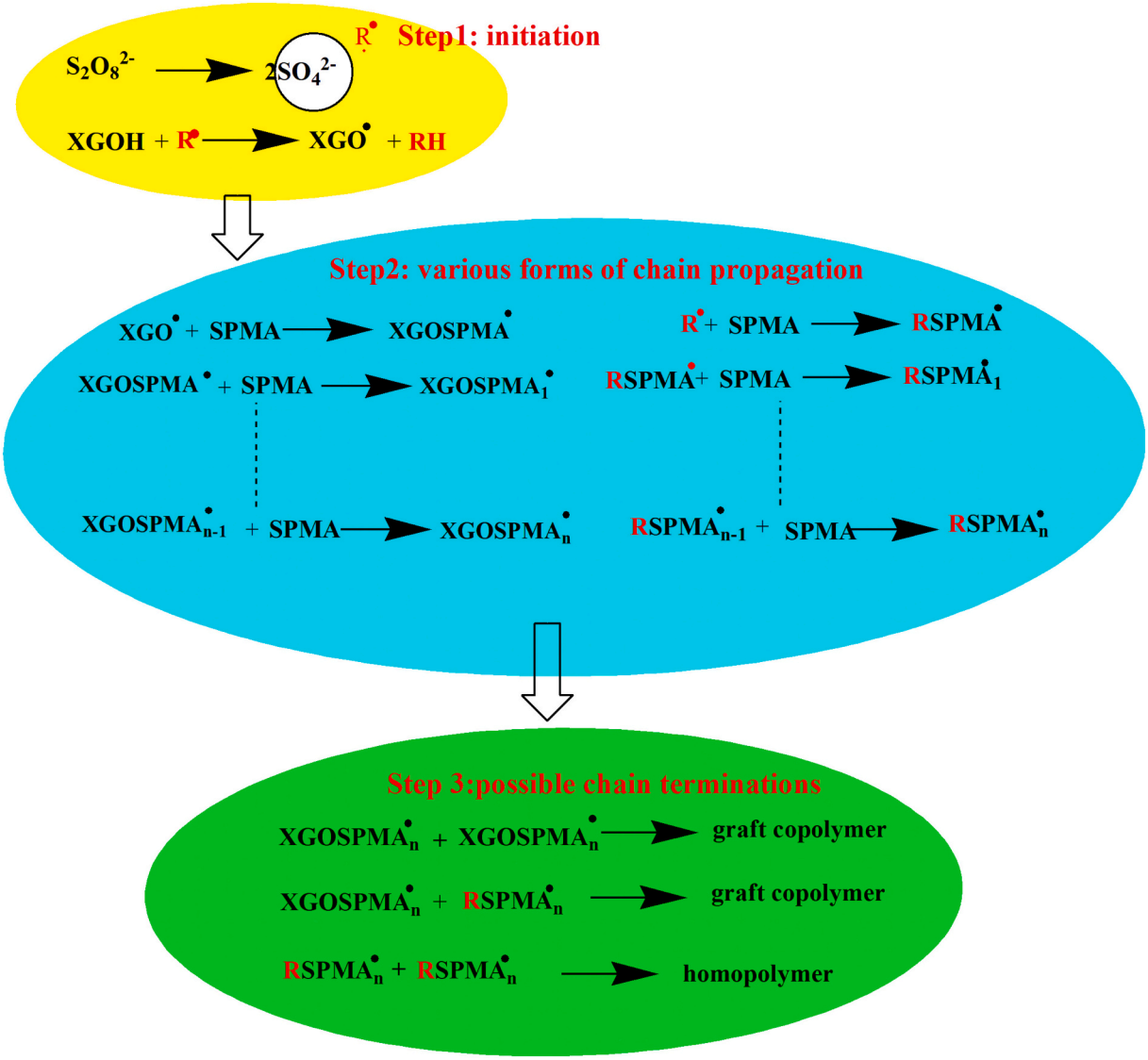

Fig. 2. Possible mechanism for formation of XG/PSMA by free radical graft copolymerization.

grafting efficiency. Similar trends have been observed in other systems reported in the literature [43,44].

To characterize changes in functional groups during the preparation of mXG/PSPMA, FTIR spectra were obtained and compared with those of XG/PSMA. As shown in Fig. 3a, the characteristic bands of XG/PSMA and mXG/PSPMA originate from both XG and PSPMA. The bands at approximately 3438, 2912, 1706, 1604, 1369, 1000–1140, and 650–1000 cm^{-1} are attributed to various stretching vibrations: O—H and -CH groups, the -C=O stretching mode in XG, asymmetric and symmetric stretching of carboxylate groups, primary OH, ketone, -C–O groups in ketals, and glycosidic bonds in XG chains [45,46]. The bands at 1033 and 601 cm^{-1} can be attributed to S=O and S—O stretching vibrations, respectively [42]. Notably, the prominent band at 536 cm^{-1} in the mXG/PSPMA spectrum corresponds to Fe—O vibration in the crystalline lattice of Fe_3O_4 which is compatible with the SEM-EDS spectrum (Supplementary Data, Fig. S3). A shift to lower wavenumbers due to the strong interaction of Fe(III)/Fe(II) ions through hydrogen bonding during the magnetization process, which occurs alongside the polymerization reaction, thereby affecting the absorption band of the hydroxyl group and broadening of the O—H band in mXG/PSPMA was also observed.

Fig. 3b shows the thermal degradation behavior of XG/PSPMA and mXG/PSPMA. The XG/PSPMA exhibits a significant weight loss at lower temperatures, indicating a lower thermal stability. The decomposition process likely involves the moisture loss or dehydration (~100–150 °C), breakdown of polymer chains and oxidation reactions (~200–300 °C), leading to a faster decline in mass. In contrast, the mXG/PSPMA composite retains a higher percentage of its weight (~60 %) compared to non-magnetic counterpart (~30 %) across the temperature range, indicating improved thermal stability (Supplementary Data, Fig. S4). The slower degradation rate can be attributed to the presence of magnetic nanoparticles, which interact with the polymer matrix, forming a more thermally stable structure. These nanoparticles may also serve as physical barriers, limiting heat transfer and thereby slowing the volatilization and degradation of polymer chains. Additionally, the presence of magnetic nanoparticles could contribute to enhanced crosslinking or intermolecular forces within the polymer matrix, further improving its resistance to thermal decomposition [47]. The incorporation of magnetic nanoparticles into the XG/PSPMA composite significantly improves its thermal stability, making it a more robust material for applications requiring high-temperature resistance. This suggests that magnetization could be a viable strategy for enhancing the durability and performance of polymer-based materials in thermal environments.

X-ray diffractograms of XG/PSPMA and mXG/PSPMA are presented in Fig. 3c. The XG/PSPMA exhibits distinct signals at 19.46°, 32.02°, 45.72°, 56.8°, 66.44°, and 75.46°, indicating partial crystallinity. [48–50] Upon magnetization, the crystalline planes of the polymeric structure is observed at 2θ = 20.74° [51], alongside signals at 2θ =

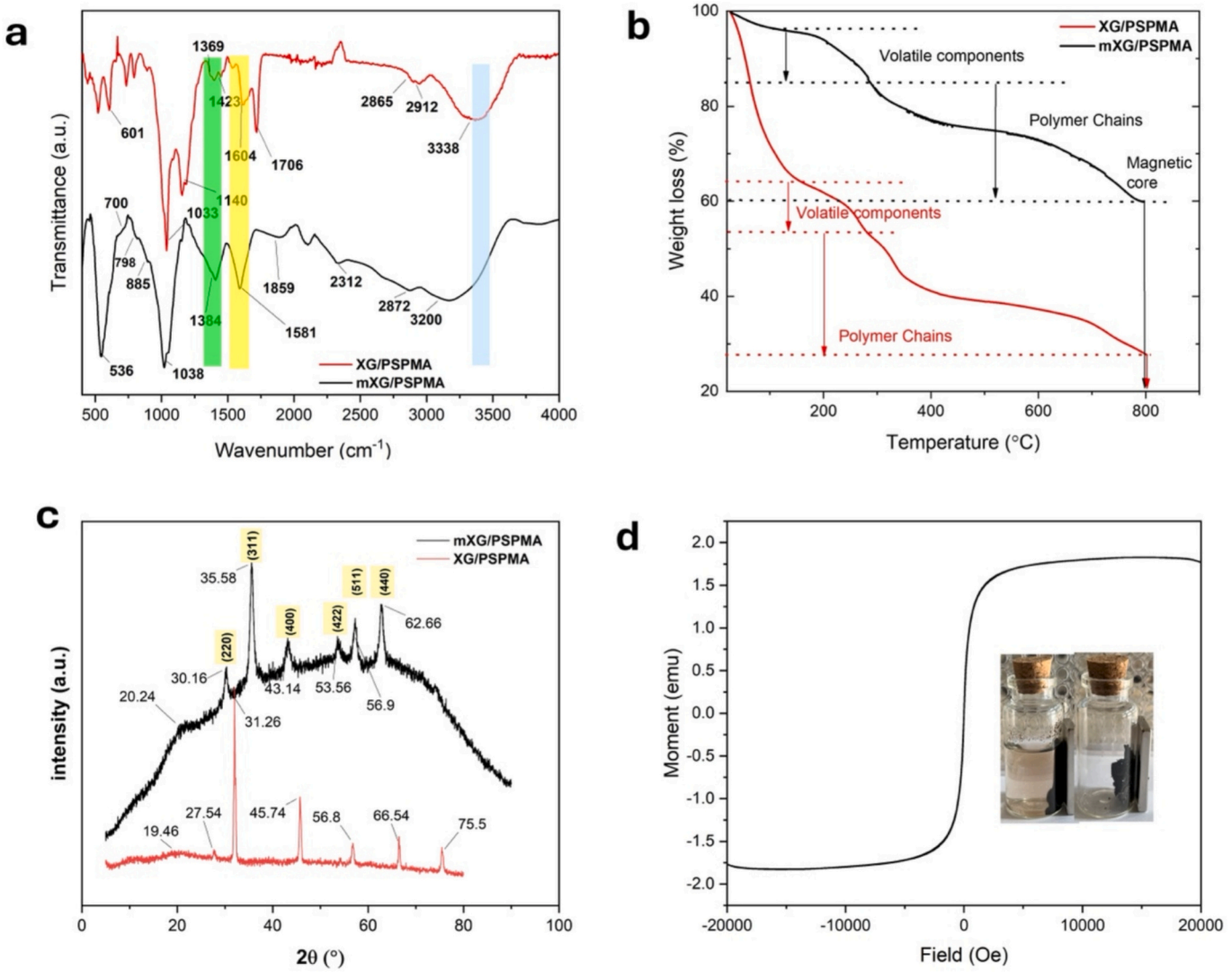

Fig. 3. FTIR spectra (a), TGA curve (b), XRD pattern (c) of XG/PSPMA and mXG/PSPMA, and VSM analysis of mXG/PSPMA.

30.24°, 35.62°, 43.16°, 53.58°, 57.16°, and 62.66°, which align with the (220), (311), (400), (422), (511), and (440) Bragg reflections, indicating that the face-centered cubic crystal structure of Fe_3O_4 [52,53]. The broadening of diffraction signals and an increase in background intensity suggest a higher degree of amorphous content in the mXG/PSPMA. This transformation indicates structural rearrangement, potentially enhancing the flexibility of polymer network and increasing the availability of active sites for adsorption. Furthermore, the mXG/PSPMA exhibits improved potential for wastewater treatment applications by combining magnetic separability.

Fig. 3d demonstrates the magnetic hysteresis curve of the mXG/PSPMA, which shows continuous and stable responses with smooth cycles in response to the applied magnetic field. The specific saturation magnetization value was 38.075 emu/g (1.82 emu). The high saturation magnetization facilitates the efficient separation of mXG/PSPMA from aqueous solutions using a simple magnet. Notably, the saturation magnetization of polymeric nanoparticles containing Fe_3O_4 varies depending on the thickness of the polymer layer encapsulating the magnetic core and the characteristics of the coating polymer, such as its molecular weight [51].

The shape, surface morphology, and composition of mXG/PSPMA are shown in Fig. 4a, with SEM micrographs at different magnifications (100×, 2.50 k×, and 500 k×) revealing that the particles have an irregular morphology and polyhedral shape due to aggregation. Moreover, the mXG/PSPMA exhibits a rough surface morphology, with the magnetic core homogeneously integrated into the polymer structure without any phase separation. The magnetic core and polymer matrix appear to form layered structures within the particle cross-section, likely due to the dense intermolecular interactions within the polymer chains. Additionally, the presence of abundant voids in the fabricated hybrid material is expected to enhance its specific surface area. mXG/PSPMA exhibited a BET surface area of 46.68 m^2/g, a pore volume of 0.148 cm^3/g, and a pore diameter of 3.9 nm, indicating that the material contains a combination of micro- and mesopores. The EDS mapping and spectrum (Supplementary Data, Fig. S3) confirm the homogeneous distribution of Fe_3O_4 on the mXG/PSPMA composite. Consistent observations were reported by Rahmatpour et al., [45] who produced XG nanoparticles containing SiO_2 via in situ synthesis, and by Pandey and Mishra [54], who developed an ethyl acrylate-xanthan gum graft copolymer. Additionally, researchers have noted that the surface of XG, before polymer grafting or coating, exhibits a smooth, homogeneous, and continuous morphology, free from cracks and discontinuities [45]. Therefore, grafting PSPMA, which contains sulfonyl groups, onto the XG surface offers multiple advantages, including (i) the introduction of sulfonic acid groups in addition to carboxyl groups, enhancing adsorption capacities, and (ii) the generation of a rough and porous morphology that increases surface area and active sites, thereby improving the suitability of materials for pollutant removal.

TEM micrographs of mXG/PSPMA, as shown in Fig. 4b, reveal nearly spherical and homogeneous particles with a heterogenous morphology, distinctly exhibiting both polymeric and inorganic phases. The lighter, amorphous regions in the micrographs correspond to voids formed by the polymer layer and intermolecular interactions, while the darker regions, attributed to Fe_3O_4 core, indicate the heavier inorganic phase due to its higher electron density. The nanocomposites exhibit a uniform particle size distribution, with average diameter of 4.98 ± 1.17 nm, as shown in histogram (Fig. 4b). Additionally, the SAED pattern confirms the presence of polycrystalline phases, consistent with XRD analysis (Fig. 3c), and attributed to the integration of XG and Fe_3O_4. These results highlight the successful synthesis of a hybrid material well-distributed phases, enhancing its structural integrity and functional properties for adsorption applications.

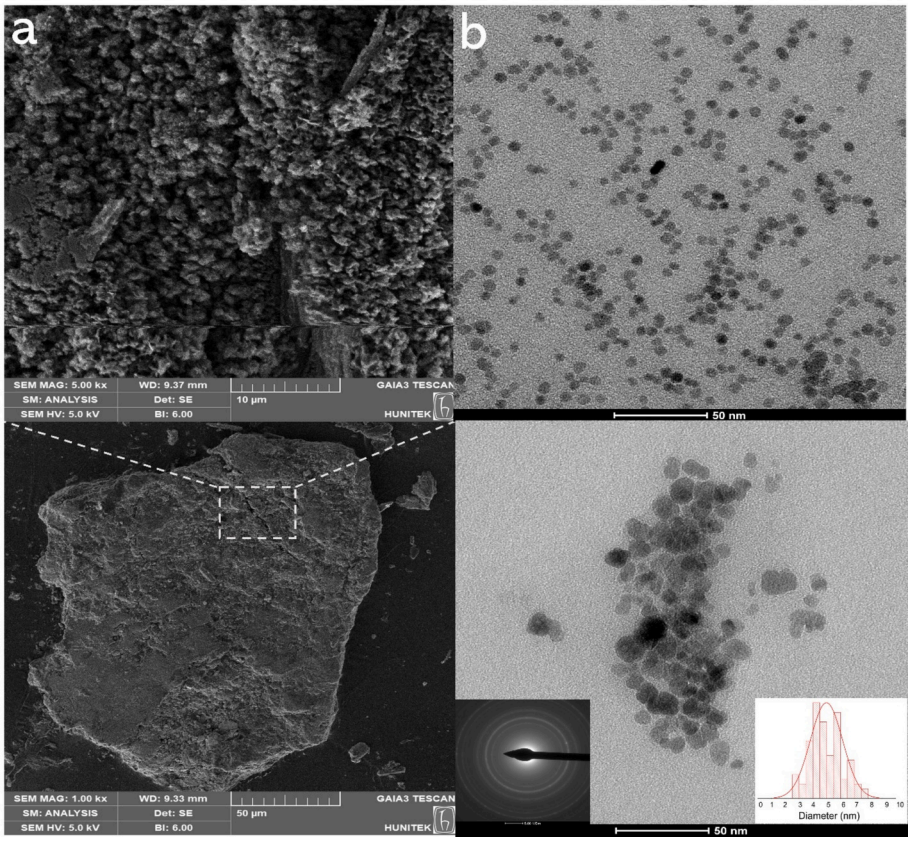

Fig. 4. SEM (a) and TEM micrographs (b) of mXG/PSPMA at different magnifications. The TEM panel (b) also shows diameter distribution and the selected area electron diffraction (SAED) pattern.

3.2. Effect of different operational conditions on adsorption performance

Fig. 5 illustrates the impact of several variables on the MB adsorption capacity of mXG/PSPMA. The MB adsorption capacity increases from 43.5 mg/g to 48.49 mg/g as the solution pH rises from 2 to 9, with minimal changes observed at higher pH values (pH 9–12), indicating pH-independent behavior, as shown in Fig. 5a. The adsorption is influenced by the degree of ionization of the functional groups of adsorbents, which varies with the pH of the medium [55]. This pH-independent behavior is attributed to the ionization of the functional groups on the mXG/PSPMA surface, the carboxyl groups tend to be predominantly existed in the -COOH form (pKa = 4.2) at low pH values (pH $\leq$ 5), whereas sulfonyl groups maintain a stable negative charge across a broad pH range due to their pKa of 0 [56], facilitating both electrostatic and hydrogen bonding interactions with MB molecules. Consequently, the adsorption between mXG/PSPMA and MB molecules occurs through electrostatic forces hydrogen bonding, and π-π interactions which persist across a wide pH range [57] **(**Fig. 5b**)**. The slight decrease in adsorption capacity observed under more alkaline conditions may be attributed to the weakening of hydrogen bonding interactions due to the imbalance in hydrogen and hydroxyl ion concentrations, as well as electrostatic repulsion caused by an excessive increase in hydroxyl ions. To gain further insight of both structural and morphological changes in mXG/PSPMA, FTIR and SEM/EDS analysis were performed after MB adsorption. The FTIR spectrum of mXG/PSPMA (Fig. 5b-**1**) reveals interactions between MB molecules and the functional groups. The O—H band shifts from 3438 to 3286 cm^{-1} and broadens, suggesting hydrogen bonding. The disappearance of the -C=O band (1706 cm^{-1}) points to electrostatic or π-π interactions with MB, while the appearance of a C—N band at 1313 cm^{-1} likely arises from adsorbed MB [10]. Additionally, shifts in the S=O (from 1033 to 1016 cm^{-1}) and S—O (from 601 to 860 cm^{-1}) bands imply MB involvement with sulfur-containing groups. The persistence of the Fe—O bond confirms the stability of the magnetic properties. The visual representation of adsorption and magnetic separation process of MB using an mXG/PSPMA composite is depicted in Fig. 5b-2**,** highlighting the efficiency of the mXG/PSPMA composite in MB removal and its magnetic responsiveness for simple and effective wastewater treatment. The SEM micrograph of the mXG/PSPMA composite in Fig. 5b-3 exhibits a smoother and more compact morphology after MB adsorption, indicating the successful attachment of MB molecules onto the composite compared to its structure before MB adsorption in Fig. 4a. The change in morphology suggests strong interactions between MB and the functional groups of mXG/PSPMA, confirming effective adsorption. Fig. 5b-4 and 5b-5 present the N_2 adsorption–desorption isotherms and the corresponding pore size distribution plots, respectively. After MB adsorption, the BET surface area decreased significantly from 47 to 30 m^2/g, indicating a substantial reduction in accessible surface sites. Similarly, the total pore volume (BJH adsorption) decreased from 0.148 to 0.133 cm^3/g, while the micropore volume (DR method) dropped more drastically from 0.016 to 0.007 cm^3/g, highlighting that micropores are preferentially occupied by MB molecules. In addition, the average pore diameter (BJH adsorption) shifted from 3.9 to 3.5 nm, and the micropore width (DR method) contracted from 2.89 to 1.53 nm, confirming pore filling and partial pore blockage upon MB uptake. These results indicate that MB adsorption occurs predominantly in the microporous network, which explains the pronounced loss in micropore volume and surface area. While mesopores also exhibit a reduction in available volume, their larger dimensions render them less severely affected. The pore structure analyses strongly support that the sorbent adsorbs MB efficiently, with preferential localization in the microporous domains. The effect of mXG/PSPMA dosage on MB removal is shown in Fig. 5c, where the mXG/PSPMA dosage increased, the adsorption efficiency improved due to the increase in the adsorption-friendly sites on the adsorbent, eventually reaching an equilibrium. The equilibrium adsorption efficiency of MB (at 50 mg of mXG/PSPMA) was 98.04 %.

Fig. 5d and e demonstrate how MB adsorption alters the colloidal properties of mXG/PSPMA in a pH-dependent manner. The hydrodynamic radius (R_H), polydispersity index (PDI), and zeta potential in relation to MB adsorption are presented in Supplementary Data (Table S1). R_H and PDI shifts after MB adsorption reveal pH-dependent structural changes in mXG/PSPMA, driven by electrostatic interactions and conformational adjustments. At pH 2, R_H decreases slightly from 590 nm to 504 nm due to limited MB binding to protonated -SO_3H, while at pH 5 (near -COOH pKa), R_H drops sharply (from 904 nm to 302 nm) as MB^+ neutralizes -COO^-, reducing aggregation. For pH 7–11, R_H stabilizes at ~360 nm (reduced from 715 nm to 887 nm) with improved PDI (0.36–0.42), indicating MB-induced stabilization via charge neutralization, steric hindrance, and hydrogen bonding (O—H shift, -C=O loss in Fig. 5b-1). The zeta potential trends also support the changes in R_H, maintaining negativity upon MB adsorption, particularly at pH > 4.5, where electrostatic MB^+/-COO^- binding dominates. Thus, MB transforms mXG/PSPMA from an aggregated state into a stabilized dispersion, with optimal effects at pH 5–7, aligning with the deprotonation of carboxyl groups and FTIR-confirmed interactions.

3.3. Simulation of real water systems

Different water systems can influence the adsorption performance of materials by altering the surrounding microenvironment [58]. The qe and R% values of MB at various concentrations in tap water were lower than those observed in deionized water (Supplementary Data, Fig. S5). This reduction is mainly due to the presence of ions in tap water, which compete with MB molecules [59] for the active binding sites on the mXG/PSPMA. The efficiency of the mXG/PSPMA was further evaluated in presence of C+, HMIs, DMix, EDCs, and their mixture, mimicking real-world conditions.

3.3.1. Effect of C+ and HMIs on MB adsorption

Despite the presence of C+ (Fig. 6a) and HMIs (Fig. 6b) across tested concentrations, mXG/PSPMA retained robust MB adsorption percentage (>87 % efficiency), demonstrating remarkable selectivity. The minimal decrease in adsorption capacity is attributed to the charge shielding effect of cations like Na^+ and K^+, which reduces electrostatic attraction and other interaction forces between the adsorbent and MB [60]. However, heavy metal ions such as Cu^{2+} and Fe^{3+} had negligible impact, likely due to concentration difference between MB and these ions typically found in concentrations ranging from 0.003 mg/L to 5 mg/L in wastewater [61]. Competitive ions can negatively affect MB adsorption by competing for adsorption sites, altering surface properties, and influencing electrostatic and chemical interactions. However, in our study, the effect of various C+ and HMIs at different concentrations on the interactions between the adsorbent and MB was found to be negligible. A similar observation was reported in previous studies, where ions like Ca^{2+} and Mg^{2+} enhanced the CR removal capacity of a cellulose-based aerogel by promoting dye coagulation [59]. This effect may also apply here, as the competitive interactions between metal ions (such as Fe^{3+}, Cu^{2+}, and Zn^{2+}, which have an affinity for carboxyl groups) and dye molecules did not significantly alter the removal capacity.

3.3.2. MB adsorption performance in DMix

The performance of mXG/PSPMA was also examined toward different cationic and anionic dyes. As shown in Fig. 6c, mXG/PSPMA demonstrated notable adsorption efficiency for MB at various concentrations, reaching MB removal efficiencies of 77.5 %, 75.3 %, and 72.45 % for 5, 10, and 50 mg/L, respectively. Among other cationic dyes, the mXG/PSPMA exhibited lower adsorption efficiency for MG (25 % removal at an initial concentration of 50 mg/L) compared to RB (85 % removal efficiency at 50 mg/L). This difference in performance may be attributed to the geometries and functional groups of the dye molecules. For instance, the higher adsorption performance of RB could be linked to the presence of positively charged $N^{\oplus}$ groups in its structure [62,63], as

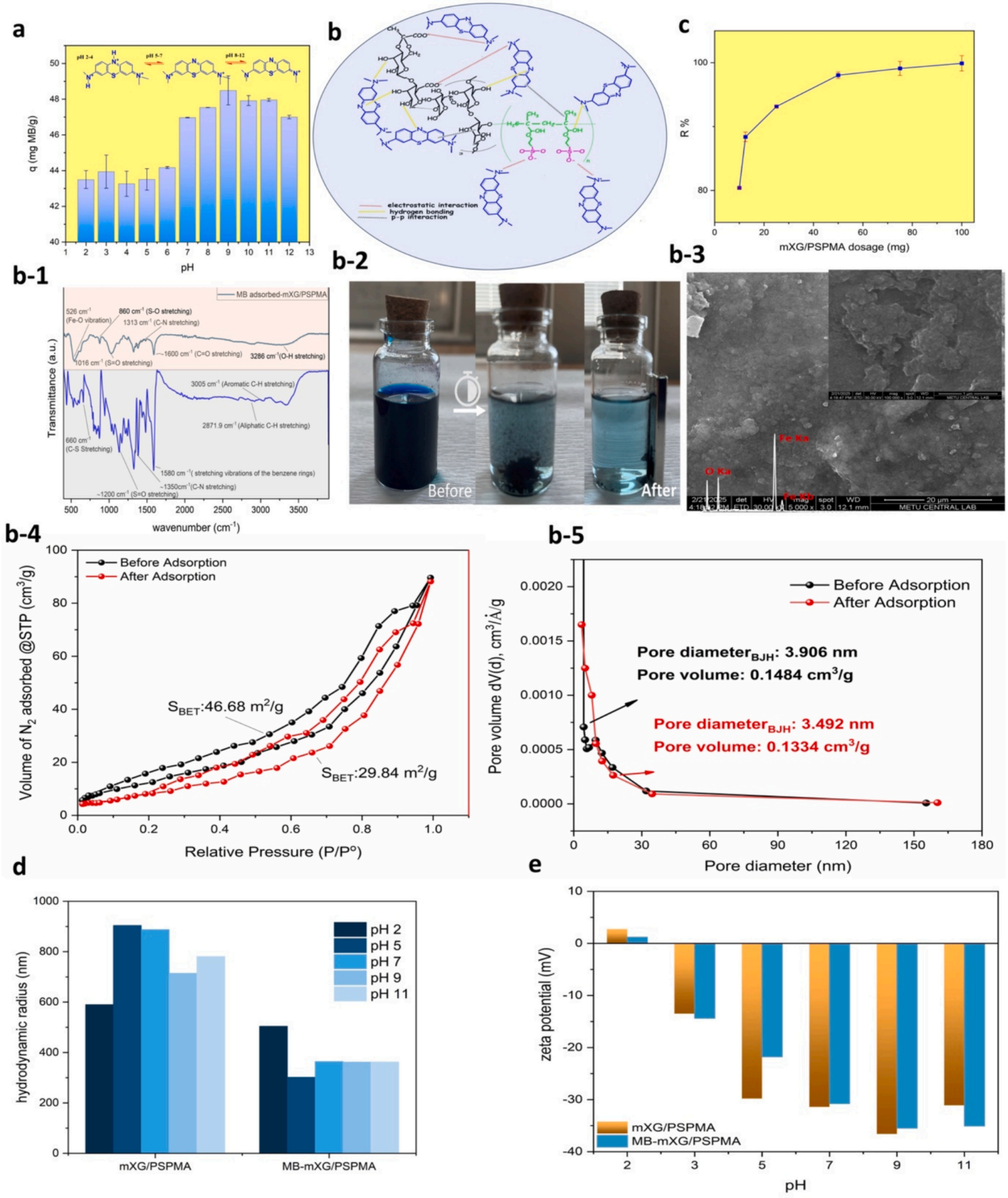

Fig. 5. Adsorption performance of mXG/PSPMA for MB under various conditions: effect of pH (a), proposed adsorption mechanism (b), including FTIR characterization (b-1), colorimetric change and magnetic separation (b-2), SEM/EDS analysis (b-3), N_2 adsorption-desorption isotherm (b-4), and pore volume versus pore size distribution plot (b-5), effect of adsorbent dosage (c), hydrodynamic radius (d), and zeta potential (e). (Conditions: pH 7; dosage = 50 mg; volume = 25 mL; incubation time = 30 min; temperature = 298 K).

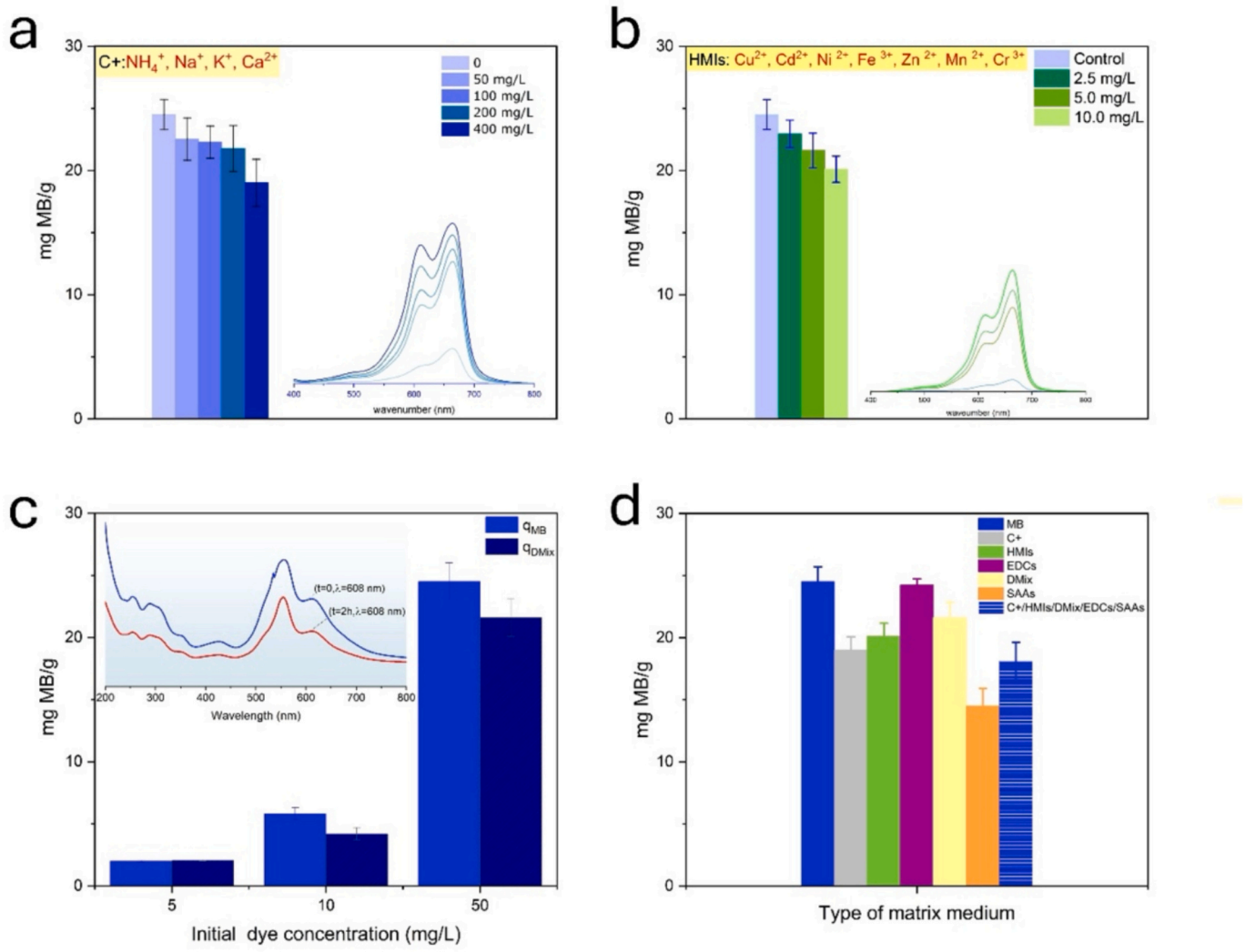

Fig. 6. Effect of C+ (a), HMIs (b), DMix (c), and complex pollutant mixtures (d) (including (a), (b), (c), EDCs, and SAAs) on MB adsorption. (Conditions: pH 7; MB concentration = 50 mg/L; dosage = 50 mg; volume = 25 mL; incubation time = 30 min; temperature = 298 K). The inset figures show UV spectra after MB adsorption.

well as additional hydrogen bonding interactions resulting from free oxygen-rich groups [64]. The larger molecular weight and complex structure of other dyes like RB-4 may lead to the occupation of more adsorption sites, while the repulsive interactions between the nanocomposite and anionic dyes (such as IC or CR) likely contribute to their relatively lower adsorption rates [65].

3.3.3. Adsorption behavior of MB under co-existing EDCs and/or HMIs

To evaluate selectivity, the affinity of mXG/PSPMA for EDCs (ibuprofen, paracetamol, carbamazepine) and HMIs was tested across pH and concentration gradients (Supplementary Data, Fig. S6). The adsorbent showed pH-dependent selectivity: paracetamol (pKa ~9.5) [66] exhibited the highest adsorption (~26 mg/g), followed by carbamazepine (pKa ~13.9, ~23 mg/g) [67] and ibuprofen (pKa ~4.91, ~5 mg/g) [68]. Zeta potential data revealed this trend stems from electrostatic interactions—the negatively charged surface (pH 5–11) repelled anionic ibuprofen while attracting neutral/positively charged paracetamol and carbamazepine as they deprotonated at higher pH. Solvent effects further modulated adsorption: ibuprofen's low capacity (0.1 mg/mL in 0.1 M NaOH) contrasted with paracetamol's performance (1 mg/mL in water) and carbamazepine's intermediate uptake (0.1 mg/mL in MeOH/water). These results demonstrate mXG/PSPMA's ability to discriminate pollutants based on charge, pH, and solvent environment.

In the case of MB, the high selectivity of mXG/PSPMA can be attributed to a combination of electrostatic attraction and specific molecular interactions. At working pH values (typically above pH 5), the surface of mXG/PSPMA is negatively charged due to deprotonation of –SO_3H and –COOH groups, while MB remains positively charged, promoting strong electrostatic interactions. Moreover, π–π stacking occurs between the aromatic rings of MB and the PSPMA backbone, enhancing selective affinity. Hydrogen bonding between MB and surface –OH or –SO_3H groups may also contribute to the interaction. This synergistic effect of charge complementarity, π–π interactions, and hydrogen bonding underlies the superior selectivity of mXG/PSPMA toward MB over other competing pollutants.

For HMIs (Cu^{2+}, Cd^{2+}, Ni^{2+}, Fe^{3+}, Zn^{2+}, Mn^{2+}, Cr^{3+}) at their optimum pH values, the oxygen-rich surface (hard base) preferentially adsorbs hard and borderline Lewis acids—explaining the strong uptake of Fe^{3+} (hard acid) and Cr^{3+}/Cu^{2+}/Ni^{2+}/Zn^{2+} (borderline acids) via stable coordination with oxygen donors (e.g., $–COO^{-}$, —O) according to the Hard and Soft Acids and Bases principle. In contrast, softer acids like Cd^{2+} and Mn^{2+} exhibit weaker adsorption.

3.3.4. MB adsorption performance in complex mixtures

Fig. 6d shows the effect of effect of C+, HMIs, EDCs, DMix, SAAs on the MB adsorption performance in a complex pollutant mixture,

highlighting the synergistic interactions among all components. The adsorption performance of mXG/PSPMA remained highly consistent across various complex mixtures, with MB removal efficiencies of 99.14 % (24.51 mg/g) for MB alone, 87.28 % (19.01 mg/g) in the presence of C+, 91.74 % (20.10 mg/g) with HMIs, 98.41 % (24.29 mg/g) with EDCs, 72.45 % (21.60 mg/g) with DMix, 58.98 % (14.50 mg/g) with SAAs, and 72.53 % (18.13 mg/g) in the presence of the complex mixture. The competition between MB and other pollutants in a multi-system can be evaluated by way of the ratio q_{multi}/q_{single}, where q_{multi} is the adsorption capacity for MB in the complex mixture system and q_{single} is the adsorption capacity for MB alone. It is reported that if the qmulti/qsingle is equal to 1, indicates no competitive effects, while values below 1 signify a reduction in adsorption capacity due to the presence of other molecules [55]. The calculated q_{multi}/q_{single} values for MB were 0.591 SAAs, 0.775C+, 0.820 HMIs, 0.881 DMix, and 0.988 EDCs, and 0.739 in the presence of all multi-pollutants combined, indicating that MB adsorption by mXG/PSPMA is adversely affected by coexisting pollutants. SAAs caused the largest reduction in MB adsorption, likely due to their strong adsorption onto mXG/PSPMA surfaces, blocking active sites, altering surface charge, and forming micelles that encapsulate MB. In contrast, EDCs had almost no effect, probably because they interact weakly with MB binding sites, occur at lower aqueous concentrations, and adsorb via different mechanisms that do not significantly hinder MB uptake. This trend demonstrates mXG/PSPMA's hierarchical adsorption preference: (1) MB's cationic charge dominates electrostatic binding to $-COO^-/-SO_3^-$ groups, (2) its planar structure enables π-π stacking even in the presence of competitors, and (3) porous nature of the *magnosorbent* provides abundant accessible sites. The retained high efficiency (>72 %) in complex systems underscores its real-world applicability.

3.3.5. Structural and chemical characterization of mXG/PSPMA after adsorption

The characterization of mXG/PSPMA after MB adsorption reveals key interactions with co-pollutants demonstrated in Supplementary Data (Fig. S7). SEM micrographs reveal how MB adsorption alters morphology of mXG/PSPMA, showing surface deposition of pollutants (EDCs as sparse aggregates, HMIs as dense particles) and pore-clogging layered deposits in complex mixtures. These structural modifications, combined with EDS elemental analysis, correlate with the retained adsorption efficiency of *magnosorbent*. Additionally, FTIR spectra indicate significant structural changes in mXG/PSPMA after MB adsorption in different conditions (Supplementary Data, Fig. S8). The characteristic band at 3276 cm^{-1}, attributed to O—H stretching, decreases in intensity, suggesting interactions with MB and other pollutants. The bands at 538 cm^{-1} (Fe—O), 877 cm^{-1} (S—O), 1008 cm^{-1} (S=O), and 1313 cm^{-1} (C—N) exhibit notable shifts and intensity variations, indicating chemical interactions and possible bonding with MB, EDCs, and HMIs. The C=O band around 1700 cm^{-1} also shows changes, implying modifications in functional groups.

XRD pattern of mXG-PSPMA several noticeable changes can be observed after MB adsorption (Supplementary Data, Fig. S9). The main crystalline signals of the composite (at $2\theta \approx 30.22°$, 35.7°, 43.28°, 53.8°, 57.32°, and 62.82°) are still present, indicating that the crystal structure of the inorganic phase remains largely intact. However, the baseline intensity in the low-angle region (10–25°) shows a more pronounced broad hump, particularly around 19.54° (highlighted in the red circle), which suggests the presence of amorphous MB molecules adsorbed onto the composite surface. This increased background and slight broadening of signals indicate partial surface coverage or intercalation of MB, which may reduce the overall crystallinity of the composite. Additionally, a slight decrease in relative intensity of the main signals and minor shifts in 2θ positions can be attributed to molecular interactions between MB and the functional groups of mXG-PSPMA, possibly through π–π stacking and electrostatic interactions, leading to subtle lattice strain.

3.4. Studies on adsorption rate and mechanism

3.4.1. Impact of time on adsorption and kinetic analysis

To understand the adsorption mechanism, the experimental data were initially fitted to common kinetic models, including the pseudo-first-order (PFO) and pseudo-second-order (PSO) models, provided in Supplementary Data (Text S3) as Eqs. 1 and 2, respectively. The fitting curves and corresponding parameters for MB adsorption at a concentration of 50 mg/L are summarized in Fig. 7a and Table S2 in Supplementary Data. The correlation coefficient (R^2) and the fit of the experimental data obtained with the PSO kinetic model are higher than those of the PFO model, suggesting that the adsorption mechanism of MB onto mXG/PSPMA is primarily governed by electrostatic attractions, hydrogen bonding, and van der Waals forces [59,69]. It can be derived that MB adsorption onto mXG/PSPMA occurs in two distinct phases: an initial rapid diffusion followed by equilibrium, with the process being notably fast. During the first phase, MB molecules rapidly diffuse to the nanoparticle surface due to intermolecular attraction forces, occupying the abundant active sites and resulting in 86.25 % removal of a 50 mg/L MB solution within the first 5 min. Equilibrium is reached within 30 min, after which extending the contact time does not significantly enhance the adsorption process. The rapid adsorption phase highlights the abundance of available adsorptive sites, which gradually become saturated over time, leading to equilibrium. Beyond this point, further increases in contact time result in minimal improvement in MB removal due to the saturation of sorption sites, as similarly reported by Li et al. [70]. Moreover, prolonged contact time leads to the aggregation of MB molecules, clogging the sorption sites and hindering further diffusion into the material as noted by Chandarana et al. [71].

3.4.2. Influence of concentration on adsorption behavior and isotherms

The effect of initial MB concentration on its adsorption by mXG/PSPMA was investigated. According to Fig. 7b, the equilibrium adsorption capacity (qe) increased rapidly at lower concentrations but, exhibited a slower growth rate as the adsorption sites on the mXG/PSPMA surface became saturated. The maximum adsorption capacity of mXG/PSPMA was determined to be 235 mg/g under the intended experimental conditions, indicating the initial concentration serves as the driving force for the MB-mXG/PSPMA adsorption process. To better understand the functionality and affinity of mXG/PSPMA for MB, the experimental data were analyzed using the Langmuir, Freundlich, and Dubinin-Radushkevich (D-R) isotherm models. All the corresponding equations and parameters were listed in Supplementary Data (Text S3, Eqs. 3–8). These models offer insights into the interactions between adsorbates and adsorbents, as well as the distribution of adsorbates between the liquid and solid phases until equilibrium is established [72,73]. The parameters obtained from these models are presented in Supplementary Data (Table S3) and the fitting curves are shown in Fig. 7b. For MB adsorption on mXG/PSPMA, all isotherm models showed a good fit with the experimental data at low MB concentrations, as indicated by R^2 values. However, at higher MB concentrations, the experimental data deviated from isotherm models, indicating that once the adsorption sites are filled, no further binding can occur [74]. Among the models, the Langmuir isotherm model demonstrated the best compatibility, as evidence by its low RSME and high R^2 values suggesting that MB follows a monolayer model, where each adsorption site accommodates only one molecule. The theoretical maximum adsorption capacity (qm) of 730 mg/g, calculated from the Langmuir isotherm, exceeds the mass of the adsorbent used, highlighting the potential of mXG/PSPMA as an excellent adsorbent for wastewater treatment. The discrepancy between the theoretical and experimental adsorption capacities may arise from practical test conditions, which can be influenced by factors such as limited accessibility of active sites, mass transfer resistance, and surface heterogeneity. Additionally, the K_L value being less than 1 (Table S3 in Supplementary Data) suggests the reversibility [75] of MB adsorption on mXG/PSPMA. As shown in

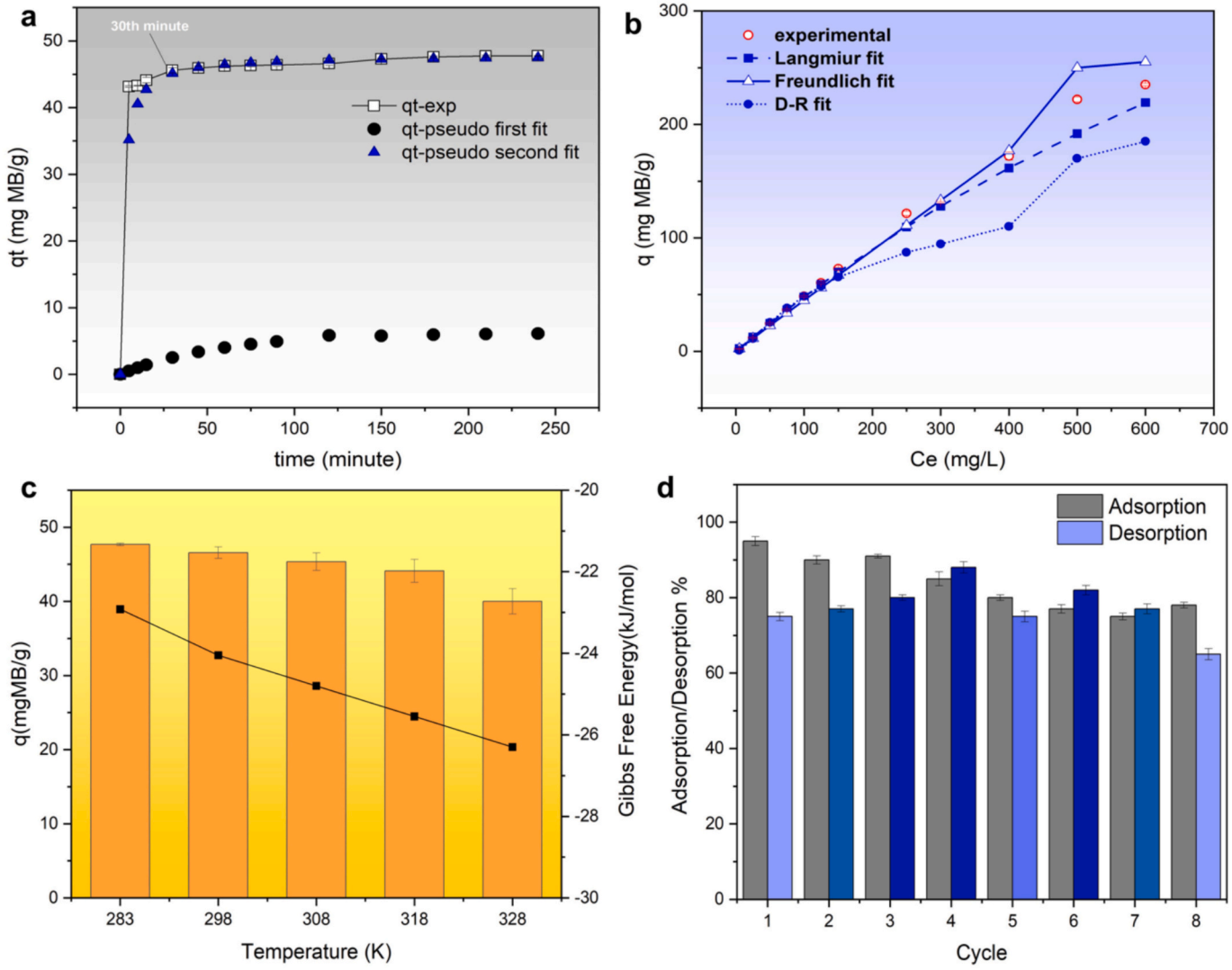

Fig. 7. Effect of incubation time on MB adsorption and adsorption kinetics fitting (a) (dosage = 25 mg; initial MB concentration = 50 mg/L), initial MB concentration on adsorption and isotherm fitting (b), temperature on MB adsorption with corresponding Gibbs free energy plots (c), and adsorption-desorption cycles of MB (d) (dosage = 50 mg; time = 30 min). (Conditions: pH 7; dosage rate = 2 mg/mL).

Supplementary Data, Fig. S10, the R_L values, which is another important parameter, derived from the Langmuir model and being less than 1, confirm that the adsorption process is favorable and occurs spontaneously [76].

The 1/n values, which classify adsorption as irreversible ($1/n = 0$), favorable ($0 < 1/n < 1$), or unfavorable ($1/n > 1$) [75,77], indicate favorable adsorption in this study ($0.1 < 1/n < 1$), suggesting the preferential binding of MB and the non-uniformity of the adsorbent sites [77–80]. Furthermore, the D-R model shows that the MB adsorption process follows physical adsorption, with a calculated binding energy was 4.08 kJ/mol, which is below the 8 kJ/mol typically associated with physical adsorption and its low energy requirements [81,82].

A comparison of maximum adsorption capacities, optimal pH values, saturation magnetization, and equilibrium times for various magnetic composites used in MB removal were presented in Table 1. The orange seed/Fe_3O_4 composite exhibited a moderate adsorption capacity of only ~22 mg/g (30–60 min, pH 8.0), which is significantly lower than that of highly functionalized materials (hundreds of mg/g), yet it maintained a relatively strong magnetic property (Ms ≈ 43 emu/g) [83]. The highest capacity reported in Table 1 is for the Fe_3O_4/chitosan-*co*-polymer system (860 mg/g, 50 min, pH 8.0), however its magnetization is extremely low (Ms ≈ 0.18 emu/g), indicating that polymer functionalization can result in a reduction in magnetization [84]. Other high performing adsorbents include carboxymethyl-cellulose/dextran sulfate (529 mg/g, 180 min, pH 7, Ms. ≈ 37.3 emu/g) [85], tannic acid-crosslinked CMC (560.9 mg/g, 120 min, pH 4.0, Ms. ≈ 10.0 emu/g) [86], and CMC/cysteine (370.4 mg/g, 60 min, pH 9.0, Ms. ≈ 75.1 emu/g) [87]. Even MOF-coated Fe_3O_4 (Fe_3O_4@SiO_2@HKUST-1) has moderate magnetization (Ms ≈ 13.7 emu/g), while achieving a high capacity of ~434.8 mg/g (90 min, pH 6–7) due to its high porosity [88]. By contrast, composites with only modest functionalization or non-ionic binders (e.g. orange seed [83], cellulose/GO [89], or Fe_3O_4/Polypyrrole/Carbon [90]) yield much lower adsorption capacities (qmax~14.4 mg/g), even though their magnetization can be relatively high (e.g., 45 emu/g for Fe_3O_4/Polypyrrole/Carbon at 90.9 mg/g). Generally, materials bearing strong anionic groups (e.g., sulfonate, carboxylate, or phenolate moieties) —such as PMAA-grafted polymers [91], sulfated CMC [87], or tannic acid [86] —exhibit significantly higher MB adsorption capacities due to the availability of electrostatic binding sites. For instance, sulfonated polymeric adsorbents such as Fe_3O_4@polypyrrole@sodium dodecyl benzene sulfonate (124.9 mg/g, pH 10.0) [92] and poly(HEMA-*co*-IA)/Fe_3O_4 (174 mg/g, pH 6.8) [93] outperform many non-modified counterparts. Kinetically, many nanocomposites reach equilibrium very quickly. GO/DETA/$MnFe_2O_4$@SiO_2 adsorbs ~243.9 mg/g in just 10 min

Table 1
Comparison of maximum adsorption capacities, pH values, magnetic saturation values, and adsorption times of magnetic composites for MB.

Adsorbents	time (minute)	pH	Saturation magnetization (Ms) Emu/g	q(mg/g)	Refs.	Adsorbents	time (minute)	pH	Saturation magnetization (Ms) Emu/g	q(mg/g)	Refs.
Orange seed/Fe_3O_4 composite	60	8.0	43.26	22.12	[83]	PEGDE-EDTA-Fe_3O_4/chitosan	30	10.0	–	5.04	[97]
Fe_3O_4/chitosan-co-polymer	50	8.0	0.178	860	[84]	Fe_3O_4 /guava leaves powder/calcium alginate	90	10.0	7.8	136.7	[98]
Fe_3O_4/CMC/dextran	180	7.0	37.33	529	[85]	MGO@TETA@MACS	240	8.0	–	247.37	[99]
Magnetic-tannic acid cross-linked carboxymethyl chitosan	120	4.0	10.0	560.92	[86]	Magnetic-AL/HAP	180	7.0	16.6	270	[100]
Magnetic CMC/cysteine	60	9.0	75.15	370.37	[87]	Poly(GMA)/Fe_3O_4–GO	70	8.0	9.75	125.95	[101]
Fe_3O_4@SiO_2@HKUST-1	90	6–7	13.7	434.78	[88]	Sulfonated Magnetic Graphene	–	7.0	28.93	–	[102]
Magnetic cellulose-g-poly (AA-*co*-AM) / GO composite	420	7.0	5.0	14.36	[89]	Aminonaphthalenesulfonic acid-Fe_3O_4-GO	240	7.0	–	286.4	[103]
Fe_3O_4/Polypyrol/Carbon	120	8.0	45.2	90.9	[90]	Magnetic zinc-polymer	140	7.0	19.07	375.93	[104]
p(MMA-co GMA)@Fe_3O_4@PMAA	150	10.0	14.57	124.9	[91]	Nano-ferromagnetic green pea biochar	10	7.0	13.302	175.44	[105]
Fe_3O_4@polypyrrole@sodium dodecyl benzene sulfonate	500	7.0	37.90	124.07	[92]	Carbon Black/Alginate-g-pAM	60	6–9	–	24.56	[106]
Fe_3O_4/Poly(HEMA-co-IA)	10	6.8	1.68	174	[93]	Fe_3O_4/poly (styrene sulfonate)-CS	60	–	–	42.21	[107]
GO/DETA/$MnFe_2O_4$@SiO_2	10	7.0	3.0	243.91	[94]	P(AMPS-co-HEMA)/AC	1440	9	–	223.39	[108]
PANI/Fe_3O_4 nanocomposite	30	12.0	5.6	61.51	[95]	β-cyclodextrin-magnetic GO	30	5.3	10.69	93.97	[109]
Carrageenan/AC	720	6.0	–	635.93	[96]	mXG/PSPMA	30	7.0	38.075	235	This study

(pH 7.0, Ms. ≈ 3.0 emu/g) [94] and PANI/Fe_3O_4 reaches ~61.5 mg/g in 30 min (pH 12, Ms. ≈ 5.6 emu/g) [95]. In contrast, some high-capacity biopolymer/AC composites require much longer contact times, for example, carrageenan/hydrochar-AC needed 720 min (12*h*) to reach 635.9 mg/g (pH 6) [96], and Fe_3O_4@ polypyrrole@sodium dodecyl benzene sulfonate took 500 min to adsorb 124.1 mg/g (pH 7) [92]. These differences matter for practical use, since shorter equilibrium times (minutes) allow faster treatment cycles, whereas multi-hour kinetics can limit throughput. Similarly, the optimal solution pH varies, with most magnetic nanocomposites performing best near neutral or slightly alkaline conditions (pH ≈ 6–8), where MB is stable and many adsorbent surfaces are negatively charged. Notable exceptions are the tannic-acid/CMC adsorbent (optimum at pH 4) [86] and PANI/Fe_3O_4 (pH 12) [95], indicating specific chemistry (e.g. protonated amines or phenolic groups) can shift the pH response. Compared to all listed systems, our novel mXG/PSPMA composite (30 min, pH 7.0, Ms. ≈ 38.1 emu/g) shows a high adsorption capacity of 235 mg/g. This qmax is lower than the absolute record (860 mg/g in Fe_3O_4/chitosan-*co*-polymer) but exceeds that of many commercial or simple composites (for instance, it is ~2.6× greater than Fe_3O_4/Polypyrrole-Carbon and ~ 4× that of Fe_3O_4/Polystyrene sulfonate-chitosan). Importantly, mXG/PSPMA combines relatively fast kinetics (30 min) with moderate-high magnetization; its Ms. ≈ 38.1 emu/g is well above most polymer-coated adsorbents, ensuring easy magnetic recovery. In summary, mXG/PSPMA offers a balanced performance, with its sulfonate-rich matrix delivering strong MB uptake comparable to or better than many literature adsorbents, while its rapid equilibrium and good magnetic response make it competitive for efficient dye removal.

3.4.3. *Influence of temperature and thermodynamic feasibility of the adsorbent*

Fig. 7c shows the effect of temperature on the MB removal efficiency of mXG/PSPMA. MB adsorption decreased with increasing temperature, from 47.67 mg/g at 283 K to 40.96 mg/g at 328 K. This approximately 20 % decrease in qe values with increasing temperature suggests that MB adsorption is more favorable at room temperature or lower. However, the decrease in adsorption is not significant enough to indicate a major negative impact of higher temperatures.

Thermodynamic parameters (ΔG, ΔH, and ΔS) were also calculated (Text S3, Eqs. 9–10). Fig. 7c also illustrates the change in ΔG values, where the negative ΔG values at all temperatures confirm the spontaneous nature of MB adsorption onto mXG/PSPMA. The continuous decrease in ΔG values with increasing temperature suggests that higher temperatures enhance the feasibility of the adsorption process. Additionally, the negative ΔH (−1651.7 J/mol) and positive ΔS (75.15 J/mol K) values indicate that the adsorption of MB on the adsorbent is exothermic and occurs with an increase in entropy [40,110].

3.5. *Regeneration, recyclability, reproducibility, and cost analysis*

Regeneration and recyclability are critical factors when assessing the effectiveness of adsorbents for wastewater treatment [111]. The recovery and reuse of dye-loaded adsorbents are especially important as they help minimize secondary solid waste, lower sorption process costs, and assist in selecting the most suitable adsorbent [112]. Among the desorbing agents tested, efficiencies were 14.92 % for citric acid, 15.31 % for NaCl, 35.10 % for acetic acid, 19.02 % for the acetic acid–ethanol mixture, and 75 % for NaOH. The superior performance of NaOH is attributed to its strong alkalinity, which effectively disrupts dye–adsorbent interactions. Fig. 7d shows that the recovery performance using NaOH over eight sorption-desorption cycles were 75 %, 77 %, 80 %, 88 %, 75 %, 82 %, 77 %, and 65 %, respectively. The observed minor drop in performance over cycles is primarily attributed to several factors: (i) partial degradation of active functional groups under repeated alkaline regeneration, (ii) leaching or chemical alteration of these groups due to harsh pH conditions, (iii) incomplete desorption of MB

molecules, and (iv) physical compaction or pore blockage of the adsorbent, which can reduce surface area and hinder diffusion. These mechanisms collectively contribute to the loss of adsorption efficiency over time. These challenges, including partial loss of sorption capacity and chemical integrity, underscore the need for improved regeneration strategies. To improve reusability, optimizing regeneration conditions using milder desorption agents (e.g., polyphenolic extracts) and reinforcing the composite structure through surface stabilization could help preserve functional groups and prolong material lifespan.

Despite these limitations, the mXG/PSPMA demonstrates remarkable reusability, proving to be a vital material for wastewater treatment. One reason for the nanocomposite's superior recovery and reusability is its magnetization property, which allows the adsorbent to be easily separated from the solution using an external magnetic field. This also provides excellent chemical stability, making the material highly effective for repeated pollutant removal. Similar observations have been reported by Swagatika et al. [113] and Zhou et al. [114]. Additionally, in one of our earlier studies, we demonstrated that PMAA-grafted magnetic cellulose nanoparticles maintained effective MB removal over 15 cycles, highlighting the potential of magnetic nanocomposites in sustainable wastewater treatment [40].

Fig. 8 demonstrates the batch-to-batch reproducibility of MB adsorption using mXG/PSPMA produced at different times. The UV spectrum of the adsorption/desorption cycle for a random batch is presented in Supplementary Data (Fig. S11), showing consistent performance across five independent production cycles (1st cycle: ~25 mg/g; 5th cycle: ~20 mg/g). The remarkably stable adsorption capacity (<25 % variation between batches) highlights the robustness of the synthesis protocol and material properties, confirming that key functional groups (-COO^-, -SO_3^-) and pore structures are reliably reproduced regardless of production time. The batch consistency (<5 % deviation from mean capacity) surpasses most reported adsorbents and is critical for industrial applications where material reproducibility is as important as performance. This trend may be due to slight differences in grafting/crosslinking, surface charge, or surface properties between batches.

The lab-scale production cost of mXG/PSPMA (~6 EUR/g, Table S4 in Supplementary Data) is offset by its high MB adsorption capacity (235 mg/g), instant magnetic separation (saving ~0.5 EUR/L in filtration costs), and multi-pollutant targeting (C+, HMIs, DMix, EDCs, and SAAs). Table S4 identifies iron source (42 % of cost) and ammonia solution (23 %) as primary cost drivers, but substituting NH_3 with NaOH reduces expenses by ~40 %. Industrial-scale production would further lower expenses through bulk reagent procurement (e.g., $FeCl_3$ at ~5× cheaper rates) and process intensification (e.g., reduced reaction time, solvent recycling). Critically, even at current pricing, reusability (>5 cycles) and selective adsorption of mXG/PSPMA make it a cost-competitive solution for complex wastewater streams.

4. Conclusion

This study demonstrates the successful synthesis, characterization, and application of *Magnosorbent* (mXG/PSPMA), a biopolymer-based magnetic nanocomposite, as a high-performance adsorbent for MB removal from complex aqueous systems. By synergistically combining the structural integrity of XG with the sulfonic acid-rich, stimuli-responsive nature of PSPMA, the nanocomposite achieves remarkable chemical stability and adaptability. The incorporation of magnetic nanoparticles further enhances its practicality, allowing for rapid and energy-efficient separation from treated water.

Magnosorbent exhibited an amorphous structure with strong magnetic properties (Ms ≈ 38 emu/g) and high surface accessibility (BET ≈ 46.7 m^2/g), enabling rapid and efficient magnetic recovery. It achieved a maximum adsorption capacity of 235 mg/g (Langmuir model) with ≥80 % MB removal within 5 min and maintained high efficiency (>98 %) across a broad pH range (2–12). Its robustness was further evidenced by sustained adsorption performance in complex multi-pollutant mixtures—including interfering cations, heavy metal ions, endocrine-

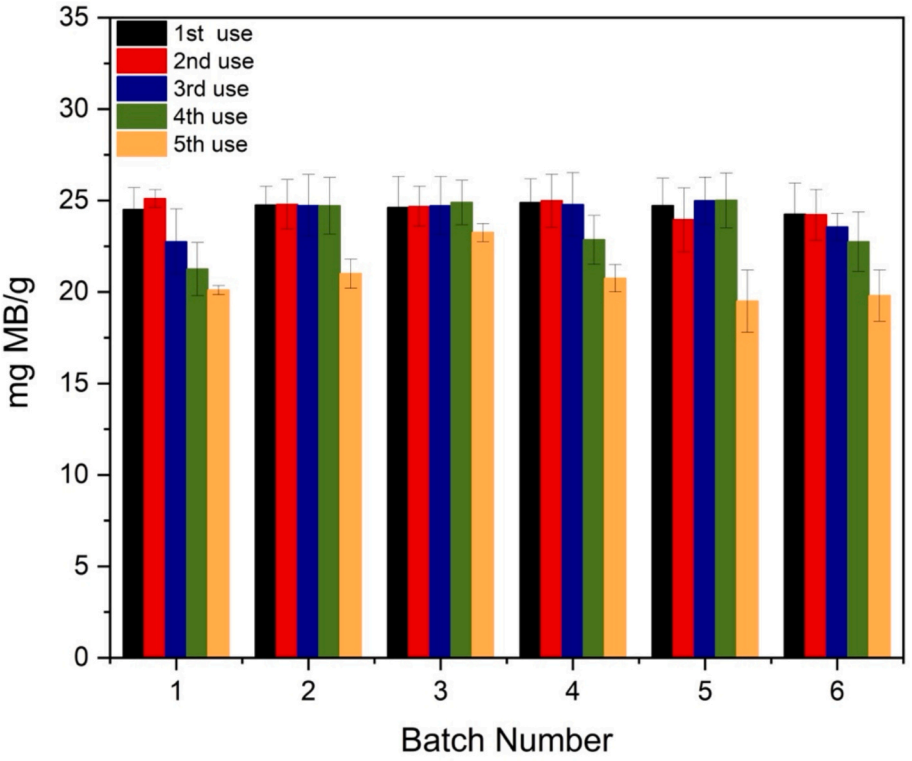

Fig. 8. Batch-to-batch reproducibility of the MB adsorption capacity for mXG/PSPMA over 5 successive cycles. (Conditions: pH 7; MB concentration = 50 mg/L; dosage = 50 mg; volume = 25 mL; incubation time = 30 min; temperature = 298 K).

disrupting compounds, dye mixtures, and surface active agents, and real water samples—retaining over 72 % removal efficiency, while hierarchical adsorption mechanisms (electrostatic attraction, π-π stacking, and porous uptake) ensured selectivity and practical applicability through ease of magnetic recovery.

Beyond its adsorption capabilities, *Magnosorbent* stands out for its sustainability and cost-effectiveness. The material retains 65–88 % removal efficiency over eight regeneration cycles, reducing operational costs and waste generation. Its batch-to-batch reproducibility (<25 % variation) and scalable synthesis further support its industrial applicability. Importantly, the use of biocompatible, naturally derived polymers aligns with green chemistry principles, offering an eco-friendly alternative to conventional adsorbents. These intrinsic advantages not only lower the environmental footprint but also provide a favorable basis for regulatory compliance and consumer acceptance.

Given these advantages, *Magnosorbent* represents a significant advancement in wastewater treatment technology, with potential applications extending beyond MB removal to the remediation of other organic pollutants, heavy metals, and emerging pollutants. Future research could explore its performance in continuous-flow systems, pilot-scale trials, and modifications for targeted pollutant removal. In addition, systematic studies on potential leaching behavior and toxicity will be essential to ensure regulatory compliance and reinforce consumer confidence in real-world applications. Furthermore, investigations into scalable synthesis routes and process economics will be critical to bridge the gap between laboratory development and industrial implementation. As industries and municipalities seek sustainable, efficient, and economically viable water treatment solutions, *Magnosorbent* emerges as a promising candidate to address the growing challenges of water pollution in an environmentally responsible manner.

CRediT authorship contribution statement

Ayşegül Ülkü Metin: Writing – review & editing, Writing – original draft, Resources, Project administration, Conceptualization. **Nesrin Horzum:** Writing – review & editing, Methodology, Formal analysis. **Abdurrahman Dağcı:** Investigation, Conceptualization. **Ahmet Tarık Savaş:** Investigation, Conceptualization.

Declaration of Generative AI and AI-assisted technologies in the writing process

While preparing this work, the authors used Grammarly to enhance the readability and language of the manuscript. After using this service, the authors reviewed and edited the content as needed and took full responsibility for the publication's content.

Declaration of competing interest

The authors declare the following financial interests/personal relationships which may be considered as potential competing interests: Aysegul Metin reports was provided by Kirikkale University Faculty of Engineering and Natural Sciences. If there are other authors, they declare that they have no known competing financial interests or personal relationships that could have appeared to influence the work reported in this paper.

Appendix A. Supplementary data

Reagents and characterization techniques utilized in the study, kinetic and isotherm model equations, calibration curves for MB and EDCs, FTIR spectra of XG/PSPMA at different SPMA concentrations, the EDS mapping and spectrum of mXG/PSPMA, DTA curve of the nanocomposites, effect of different water sample types, affinity of EDCs and HMIs, morphological and structural changes in the mXG/PSPMA after MB adsorption in the presence of EDCs, HMIs, and complex pollutant mixtures, XRD pattern of mXG/PSPMA after MB adsorption, change of R_L value of the mXG/PSPMA, representative UV spectrum of the adsorption/desorption cycle, effect of pH on R_H, PDI, and zeta potential, calculated kinetic and isotherm model constants, and cost estimation. Supplementary data to this article can be found online at https://doi.org/10.1016/j.ijbiomac.2025.147640.

Data availability

Data will be made available on request.

References

[1] M.R. Awual, Novel ligand functionalized composite material for efficient copper (II) capturing from wastewater sample, Compos. B. Eng. 172 (2019) 387–396, https://doi.org/10.1016/j.compositesb.2019.05.103.
[2] N. Bostan, N. Ilyas, N. Akhtar, S. Mehmood, R.U. Saman, R.Z. Sayyed, A. A. Shatid, M.Y. Alfaifi, S.E.I. Elbehairi, S. Pandiaraj, Toxicity assessment of microplastic (MPs); a threat to the ecosystem, Environ. Res. 234 (2023) 116523, https://doi.org/10.1016/j.envres.2023.116523.
[3] N.T. Bui, H. Kang, S.J. Teat, G.M. Su, C.-W. Pao, Y.-S. Liu, E.W. Zaia, J. Guo, J.-L. Chen, K.R. Meihaus, C. Dun, T.M. Mattox, J.R. Long, P. Fiske, R. Kostecki, J. J. Urban, A nature-inspired hydrogen-bonded supramolecular complex for selective copper ion removal from water, Nat. Commun. 11 (2020) 3947, https://doi.org/10.1038/s41467-020-17757-6.
[4] Z. Chen, J. Fang, W. Wei, H.H. Ngo, W. Guo, B.-J. Ni, Emerging adsorbents for micro/nanoplastics removal from contaminated water: advances and perspectives, J. Clean. Prod. 371 (2022) 133676, https://doi.org/10.1016/j.jclepro.2022.133676.
[5] K.Z. Elwakeel, M.M. Ahmed, A. Akhdhar, H.M. Alghamdi, M.G. Sulaiman, M. F. Hamza, Z.A. Khan, Effect of the magnetic core in alginate/gum composite on adsorption of divalent copper, cadmium, and lead ions in the aqueous system, Int. J. Biol. Macromol. 253 (2023) 126884, https://doi.org/10.1016/j.ijbiomac.2023.126884.
[6] H.M. Alghamdi, R.M. Mohammad, K.Z. Elwakeel, Simultaneous removal of Eriochrome black T and chromate anions from aqueous solution using functionalized hybrid magnetic polymers, J. Polym. Environ. 32 (2024) 6522–6543, https://doi.org/10.1007/s10924-024-03397-0.
[7] K.Z. Elwakeel, A.M. Elgarahy, M.S. Zoromba, A.S. Al-Bogami, A. Akhdhar, N. M. Mashaal, Optimizing magnetic carbon nanotube/polyaniline nanocomposite for sequestering harmful organic contaminants, Water Air Soil Pollut. 236 (4) (2025) 205, https://doi.org/10.1007/s11270-025-07825-2.
[8] I. Buhani, S. Suharso, A. Sutarto, H.M. Alghamdi, K.Z. Elwakeel, Cationic surfactant-modified *Tetraselmis* sp. for the removal of organic dyes from aqueous solution, Molecules 28 (23) (2023) 7839, https://doi.org/10.3390/molecules28237839.
[9] D. Buhani, J.S. Fajriyah, N.S. Rilyanti, M.S. Sumadi, K.Z. Elwakeel, Modification of non-activated carbon from rubber fruit shells with 3-(aminopropyl)-triethoxysilane and its adsorption study on coomassie brilliant blue and methylene blue in solution, Water Air Soil Pollut. 234 (9) (2023) 578, https://doi.org/10.1007/s11270-023-06506-2.
[10] A.M. Elgarahy, H.Y. Mostafa, E.G. Zaki, S.M. ElSaeed, K.Z. Elwakeel, A. Akhdhar, E. Guibal, Methylene blue removal from aqueous solutions using a biochar/gellan gum hydrogel composite: effect of agitation mode on sorption kinetics, Int. J. Biol. Macromol. (2023) 123355, https://doi.org/10.1016/j.ijbiomac.2023.123355.
[11] S. Buhani, M. Rilyanti, F.D.R. Antika, L.P. Lestari, K.Z. Elwakeel, Functionalization of carbon from rubber fruit shells (*Hevea brasiliensis*) with silane agents and its application to the adsorption of bi-component mixtures of methylene blue and crystal violet, Environ. Sci. Pollut. Res. 31 (28) (2024) 39994–40007, https://doi.org/10.1007/s11356-023-28031-9.
[12] A.A. Spagnoli, D.A. Giannakoudakis, S. Bashkova, Adsorption of methylene blue on cashew nut shell based carbons activated with zinc chloride: the role of surface and structural parameters, J. Mol. Liq. 229 (2017) 465–471, https://doi.org/10.1016/j.molliq.2016.12.106.
[13] M. Yang, X. Liu, Y. Qi, W. Sun, Y. Men, Preparation of κ-carrageenan/graphene oxide gel beads and their efficient adsorption for methylene blue, J. Colloid Interface Sci. 506 (2017) 669–677, https://doi.org/10.1016/j.jcis.2017.07.093.
[14] L. Ma, W. Liu, B. Liu, Y.C. Tang, Removal of methylene blue by acrylic polymer adsorbents loaded with magnetic iron manganese oxides: synthesis, characterization, and adsorption mechanisms, Chemosphere 346 (2024) 140588, https://doi.org/10.1016/j.chemosphere.2023.140588.
[15] M. Zheng, F. Ma, M. Liu, M. Li, Q. Yu, H. Zhu, H. Guo, H. Sun, Preparation and model construction of novel 2D nanocomposite of Zn-P-GCNN and its mechanisms of synergistic adsorption for cu(II) and methylene blue, J. Clean. Prod. 395 (2023) 136387, https://doi.org/10.1016/j.jclepro.2023.136387.
[16] D. Dimbo, M. Abewaa, E. Adino, A. Mengistu, T. Takele, A. Oro, M. Rangaraju, Methylene blue adsorption from aqueous solution using activated carbon of spathodea campanulata, Results Eng. 21 (2024) 101910, https://doi.org/10.1016/j.rineng.2024.101910.

[17] B. Charmas, M. Zięzio, K. Jedynak, Assessment of the porous structure and surface chemistry of activated biocarbons used for methylene blue adsorption, Molecules 28 (2023) 4922, https://doi.org/10.3390/molecules28134922.

[18] D. Mani, D. Elango, A. Priyadharsan, L.A. Al-Humai, N.D. Al-Dahmash, S. Ragupathy, P. Jayanthi, Y.-H. Ahn, Groundnut shell chemically treated with KOH to prepare inexpensive activated carbon: methylene blue adsorption and equilibrium isotherm studies, Environ. Res. 231 (2023) 116026, https://doi.org/10.1016/j.envres.2023.116026.

[19] A. Nouri, W.L. Ang, E. Mahmoudi, S.F. Chua, A. Mohammad, A. Benamor, M. M. Ba-Abbad, C.P. Leo, Decoration of polylactic acid on graphene oxide for efficient adsorption of methylene blue and tetracycline, Chemosphere 322 (2023) 138219, https://doi.org/10.1016/j.chemosphere.2023.138219.

[20] P. Samiyammal, B. Srividhya, S. Renukadevi, D. Senthil Kumar, P. Prabu, D. Mani, A.A. Ghafar, S. Ragupathy, Facile synthesis of tin-doped copper oxide loaded on almond Shell activated carbon composite for the Photodegradation of organic pollutants under sunlight, Luminescence 40 (5) (2025) e70200, https://doi.org/10.1002/bio.70200.

[21] B. Yardımcı, N. Kanmaz, An effective-green strategy of methylene blue adsorption: sustainable and low-cost waste cinnamon bark biomass enhanced via MnO_2, J. Environ. Chem. Eng. 11 (3) (2023) 110254, https://doi.org/10.1016/j.jece.2023.110254.

[22] M. Aaddouz, K. Azzaoui, N. Akartasse, E. Mejdoubi, B. Hammouti, M. Taleb, R. Sabbahi, S.F. Alshahateet, Removal of methylene blue from aqueous solution by adsorption onto hydroxyapatite nanoparticles, J. Mol. Struct. 1288 (2023) 135807, https://doi.org/10.1016/j.molstruc.2023.135807.

[23] J. Lui, Q. Lin, J. Gao, X. Jia, M. Cai, Q. Liang, Adsorption properties and mechanisms of methylene blue and tetracycline by nano-silica biochar composites activated by KOH, Chemosphere 337 (2023) 139395, https://doi.org/10.1016/j.chemosphere.2023.139395.

[24] S. Soleimani, A. Heydari, M. Fattahi, A. Motamedisade, Calcium alginate hydrogels reinforced with cellulose nanocrystals for methylene blue adsorption: synthesis, characterization, and modelling, Ind. Crop. Prod. 192 (2023) 115999, https://doi.org/10.1016/j.indcrop.2022.115999.

[25] F. Mohammadzadeh, M. Golshan, V. Haddadi-Asl, M. Salami-Kalajahi, Adsorption kinetics of methylene blue from wastewater using pH-sensitive starch-based hydrogels, Sci. Rep. 13 (2023) 11900, https://doi.org/10.1038/s41598-023-39241-z.

[26] S.-F. Sun, H.-F. Wan, X. Zhao, C. Gao, L.-P. Xiao, R.-C. Sun, Facile construction of lignin-based network composite hydrogel for efficient adsorption of methylene blue from wastewater, Int. J. Biol. Macromol. 253 (2023) 126688, https://doi.org/10.1016/j.ijbiomac.2023.126688.

[27] M.S. Kazemi, A. Sobhani, $CuMn_2O_4$/chitosan micro/nanocomposite:Green synthesis, methylene blue removal, and study of kinetic adsorption, adsorption isotherm experiments, mechanism and adsorbent capacity, Arab. J. Chem. 16 (2023) 104754, https://doi.org/10.1016/j.arabjc.2023.104754.

[28] G. Liu, Z. Liu, S. Li, C. Shi, T. Xu, M. Huo, Y. Lin, Aluminum copper bimetallic metal organic gels/sodium alginate beads for efficient adsorption of ciprofloxacin and methylene blue: adsorption isotherm, kinetic and mechanism studies, Process. Saf. Environ. Prot. 176 (2023) 763–775, https://doi.org/10.1016/j.psep.2023.05.064.

[29] L. An, S. He, J. Zhang, J. Liu, W. Shao, Preparation and characterization of novel cellulose-based adsorbent with ultra-high methylene blue adsorption performance, Mater. Chem. Phys. 296 (2023) 127261, https://doi.org/10.1016/j.matchemphys.2022.127261.

[30] J. Yang, S. Shojaei, S. Shojaei, Removal of drug and dye from aqueous solutions by graphene oxide: adsorption studies and chemometrics methods, NPJ Clean Water 5 (2022) 5, https://doi.org/10.1038/s41545-022-00148-3.

[31] A. Molla, Y. Li, B. Mandal, S.G. Kang, S.H. Hur, J.S. Chung, Selective adsorption of organic dyes on graphene oxide: theoretical and experimental analysis, Appl. Surf. Sci. 464 (2019) 170–177, https://doi.org/10.1016/j.apsusc.2018.09.056.

[32] H. Molavi, A. Shojaei, A. Pourghaderi, Rapid and tunable selective adsorption of dyes using thermally oxidized nanodiamond, J. Colloid Interface Sci. 524 (2018) 52–64, https://doi.org/10.1016/j.jcis.2018.03.088.

[33] Z. Akbari, M. Ghiaci, F. Nezampour, Encapsulation of vanadium phosphorus oxide into TiO_2 matrix for selective adsorption of methylene blue from aqueous solution, J. Chem. Eng.Data. 63 (2018) 3923–3932, https://doi.org/10.1021/acs.jced.8b00549.

[34] B. Chen, Y. Cao, H. Zhao, F. Long, X. Feng, J. Li, X. Pan, A novel Fe^{3+}-stabilized magnetic polydopamine composite for enhanced selective adsorption and separation of methylene blue from complex wastewater, J. Hazard. Mater. 3925 (2020) 122263, https://doi.org/10.1016/j.jhazmat.2020.122263.

[35] L. Zhao, M. Gao, W. Yue, Y. Jiang, Y. Wang, Y. Ren, F. Hu, Sandwich-structured graphene-Fe_3O_4@carbon nanocomposites for high-performance lithium-ion batteries, ACS Appl. Mater. Interfaces 7 (2015) 9709–9715, https://doi.org/10.1021/acsami.5b01503.

[36] G. Xie, P. Xi, H. Liu, F. Chen, L. Huang, Y. Shi, F. Hou, Z. Zeng, C. Shao, J. Wang, A facile chemical method to produce superparamagnetic graphene oxide–Fe_3O_4 hybrid composite and its application in the removal of dyes from aqueous solution, J. Mater. Chem. 22 (2012) 1033–1039, https://doi.org/10.1039/C1JM13433G.

[37] H.M. Alghamdi, A.M. Elgarahy, M.S. Zoromba, K.Z. Elwakeel, A microwave-regenerable multi-walled carbon nanotube/polyaniline/Fe_3O_4 ternary nanocomposite for quantifiable sorption of cationic and anionic dyes, Colloids Surf. A Physicochem. Eng. Asp. 698 (2024) 134438, https://doi.org/10.1016/j.colsurfa.2024.134438.

[38] Z.-W. Xie, Jie-Ci, L. Meng-Ya, X. Hua-Ying, W. Ying-Xuan, W.F.-A. He, H.-L. Jiang, Novel Fe_3O_4 nanoparticle/β-cyclodextrin-based polymer composites for the removal of methylene blue from water, Ind. Eng. Chem. Res. 59 (2020) 12270–12281, https://doi.org/10.1021/acs.iecr.0c01115.

[39] G. Sarojini, S. Venkatesh Babu, N. Rajamohan, M. Rajasimman, Arivalagan Pugazhendhi, Application of a polymer-magnetic-algae based nano-composite for the removal of methylene blue – characterization, parametric and kinetic studies, Env. Poll. 292 (2022) 118376, https://doi.org/10.1016/j.envpol.2021.118376.

[40] D. Doğan, A.H. Mohamed Ariff, Z. Leman, A.Ü. Metin, Magnetic cellulose-based composite as a new effectively reusable biosorbent for cationic dye removal: batch and lab-scale column studies, Cellulose 30 (2023) 7003–7029, https://doi.org/10.1007/s10570-023-05282-w.

[41] E. Alver, A.Ü. Metin, Chitosan based metal-chelated copolymer nanoparticles: laccase immobilization and phenol degradation studies, Int. Biodeterior. Biodegrad. 125 (2017) 235–242, https://doi.org/10.1016/j.ibiod.2017.07.012.

[42] A. Salama, Preparation of CMC-g-P(SPMA) super adsorbent hydrogels: exploring their capacity for MB removal from waste water, Int.J. Biol.Macromol. 106 (2018) 940–946, https://doi.org/10.1016/j.ijbiomac.2017.08.097.

[43] E. Makhado, S. Pandey, P.N. Nomngongo, J. Ramontja, Fast microwave-assisted green synthesis of xanthan gum grafted acrylic acid for enhanced methylene blue dye removal from aqueous solution, Carbohydr. Polym. 176 (2017) 315–326, https://doi.org/10.1016/j.carbpol.2017.08.093.

[44] C. Makhlouf, S. Marais, S. Roudesli, Graft copolymerization of acrylic acid onto polyamide fibers, Appl. Surf. Sci. 253 (2007) 5521–5528, https://doi.org/10.1016/j.apsusc.2006.12.086.

[45] A. Rahmatpour, A.H.A. Hesarsorkh, Chitosan and silica nanoparticles-modified xanthan gum-derived bio-nanocomposite hydrogel film for efficient uptake of methyl orange acidic dye, Carbohydr. Polym. 328 (2024) 121721, https://doi.org/10.1016/j.carbpol.2023.121721.

[46] R. Ahmad, M.O. Ejaz, Efficient adsorption of crystal violet (CV) dye onto benign chitosan-modified l-cysteine/bentonite (CS-Cys/bent) bionanocomposite: synthesis, characterization and experimental studies, Dyes Pigments 216 (2023) 111305, https://doi.org/10.1016/j.dyepig.2023.111305.

[47] Z. Said, A.K. Pandey, A.K. Tiwari, B. Kalidasan, F. Jamil, A.K. Thakur, H.M. Ali, Nano-enhanced phase change materials: fundamentals and applications, Prog. Energy Combust. Sci. 104 (2024) 101162, https://doi.org/10.1016/j.pecs.2024.101162.

[48] G. Liu, M. Cai, X. Wang, F. Zhou, W. Liu, Core–shell–corona-structured polyelectrolyte brushes-grafting magnetic nanoparticles for water harvesting, ACS Appl. Mater. Interfaces 6 (14) (2014) 11625–11632, https://doi.org/10.1021/am502351x.

[49] M.H.A. Elella, E.S. Goda, H. Gamal, S.M. El-Bahy, M.A. Nour, K.R. Yoon, Green antimicrobial adsorbent containing grafted xanthan gum/SiO_2 nanocomposites for malachite green dye, Int. J. Biol. Macromol. 191 (2021) 385–395, https://doi.org/10.1016/j.ijbiomac.2021.09.040.

[50] G. Sharma, A. Kumar, A.A. Ghfar, A. García-Peñas, M. Naushad, F.J. Stadler, Fabrication and characterization of xanthan gum-cl-poly(acrylamide-co-alginic acid) hydrogel for adsorption of cadmium ions from aqueous medium, Gels 8 (1) (2021) 23, https://doi.org/10.3390/gels8010023.

[51] T. Babacan, D. Doğan, Ü. Erdem, A.Ü. Metin, Magnetically responsive chitosan-based nanoparticles for remediation of anionic dyes: adsorption and magnetically triggered desorption, Mater. Chem. Phys. 284 (2022) 126032, https://doi.org/10.1016/j.matchemphys.2022.126032.

[52] S. Shabzendedar, A.R. Modarresi-Alam, M. Noroozifar, K. Kerman, Core-shell nanocomposite of superparamagnetic Fe_3O_4 nanoparticles with poly (*m*-aminobenzenesulfonic acid) for polymer solar cells, Org. Electron. 77 (2020) 105462, https://doi.org/10.1016/j.orgel.2019.105462.

[53] M. Yarmohamadi-Vasel, A.R. Modarresi-Alam, M. Noroozifar, M.S. Hadavi, An investigation into the photovoltaic activity of a new nanocomposite of (polyaniline nanofibers)/(titanium dioxide nanoparticles) with different architectures, Synth. Met. 252 (2019) 50–61, https://doi.org/10.1016/j.synthmet.2019.04.007.

[54] S. Pandey, S.B. Mishra, Graft copolymerization of ethylacrylate onto xanthan gum, using potassium peroxydisulfate as an initiator, Int. J. Biol.Macromol. 49 (2011) 527–535, https://doi.org/10.1016/j.ijbiomac.2011.06.005.

[55] A.Ü. Metin, D. Doğan, M. Can, Novel magnetic gel beads based on ionically crosslinked sodium alginate and polyanetholesulfonic acid: synthesis and application for adsorption of cationic dyes, Mater. Chem. Phys. 256 (2020) 123659, https://doi.org/10.1016/j.matchemphys.2020.123659.

[56] W. Wei, J.K. Bediako, S. Kim, Y.-S. Yun, Removal of cd(II) by poly(styrenesulfonic acid)-impregnated alginate capsule, J. Taiwan Inst. Chem. Eng. 61 (2016) 188–195, https://doi.org/10.1016/j.jtice.2015.12.009.

[57] Y. Liu, Y. Ke, Q. Shang, X. Yang, D. Wang, G. Liao, Fabrication of multifunctional biomass-based aerogel with 3D hierarchical porous structure from waste reed for the synergetic adsorption of dyes and heavy metal ions, Chem. Eng. J. 451 (2023) 138934, https://doi.org/10.1016/j.cej.2022.138934.

[58] M.R. Awual, A. Islam, M.M. Hasan, M.M. Rahman, A.M. Asiri, M.A. Khaleque, M. C.S. Heikh, Introducing an alternate conjugated material for enhanced lead(II) capturing from wastewater, J. Clean. Prod. 224 (2019) 920–929, https://doi.org/10.1016/j.jclepro.2019.03.241.

[59] W.-P. Qui, H.-Z. Su, T.-G. Hu, H. Su, N. Li, L.-S. Lai, J.-I. Zhu, Y.-L. Zhao, Z. Xu, H. Wang, P. Wen, Biodegradable taro stem cellulose aerogel: a simple approach for adsorbing microplastics and dyestuffs contaminants, J. Colloid Interface Sci. 679 (2025) 358–374, https://doi.org/10.1016/j.jcis.2024.09.202.

[60] Y. Li, S. Zhang, S. Liu, Y. Chen, M. Luo, S. Xu, X. Hou, Eco-friendly hydrophobic ZIF-8/sodium alginate monolithic adsorbent: An efficient trap for microplastics in the aqueous environment, J. Colloid Interface Sci. 661 (2024) 259–270, https://doi.org/10.1016/j.jcis.2024.01.182.
[61] R. Shrestha, S. Ban, S. Devkota, S. Sharma, R. Joshi, A.P. Tiwari, H.Y. Kim, M. K. Joshi, Technological trends in heavy metals removal from industrial wastewater: a review, J. Environ. Chem. Eng. 9 (2021) 105688, https://doi.org/10.1016/j.jece.2021.105688.
[62] H. Du, Y. Zhang, H. Jiang, H. Wang, Adsorption of rhodamine B on polyvinyl chloride, polystyrene, and polyethylene terephthalate microplastics in aqueous environments, Environ. Technol. Innov. 27 (2022) 102495, https://doi.org/10.1016/j.eti.2022.102495.
[63] W. Rao, P. Piliouras, X. Wang, A. Guido, K. Kugler, B. Sieren, L. Wang, G. Lv, Z. Li, Zwitterionic dye rhodamine B (RhB) uptake on different types of clay minerals, Appl. Clay Sci. 197 (2020) 105790, https://doi.org/10.1016/j.clay.2020.105790.
[64] Y.E. Ouardi, A.E. Aissouq, A. Chennah, A. Ouammou, K. Laatikainen, Synthesis, characterization, and DFT investigation of rhodamine B dye removal by activated carbon produced from argan nutshell, biomass conv, Bioref 14 (2024) 15107–15118, https://doi.org/10.1007/s13399-022-03706-4.
[65] H. Wang, Y. Hao, S. Chen, M. Cheng, C. Li, S. Sun, S. Hu, DFT study of imidazoles adsorption on the grain boundary of cu (100) surface, Corros. Sci. 137 (2018) 33–42, https://doi.org/10.1016/j.corsci.2018.03.009.
[66] S.P. Clissold, Paracetamol and phenacetin, Drugs 32 (1986) 46–59, https://doi.org/10.2165/00003495-198600324-00005.
[67] M. Bizi, Mohamed., Activated carbon and the principal mineral constituents of a natural soil in the presence of carbamazepine, Water 11 (11) (2019) 2290, https://doi.org/10.3390/w11112290.
[68] M. Yamin, Z.K. Ghouri, N. Rohman, J.A. Syed, A. Skelton, K. Ahmed, Unravelling pH/pKa influence on pH-responsive drug carriers: insights from ibuprofen-silica interactions and comparative analysis with carbon nanotubes, sulfasalazine, and alendronate, J. Mol. Graph. Model. 128 (2024) 108720. Yamin, https://doi.org/10.1016/j.jmgm.2024.108720.
[69] C. Qui, Q. Tang, X. Zhang, M.C. Li, X. Zhang, J. Xie, S. Zhang, Z. Su, J. Qi, H. Xiao, Y. Chen, Y. Jiang, C.F. de Hoop, X. Huang, High-efficient double-cross-linked biohybrid aerogel biosorbent prepared from waste bamboo paper and chitosan for wastewater purification, J. Clean. Prod. 338 (2022) 130550, https://doi.org/10.1016/j.jclepro.2022.130550.
[70] X. Li, C. Wang, J. Zhang, J. Liu, B. Liu, G. Chen, Preparation and application of magnetic biochar in water treatment: a critical review, Sci. Total Environ. 711 (2020) 134847, https://doi.org/10.1016/j.scitotenv.2019.134847.
[71] H. Chandarana, P.S. Kumar, M. Seenuvasan, M.A. Kumar, Kinetics, equilibrium and thermodynamic investigations of methylene blue dye removal using *Casuarina equisetifolia*pines, Chemosphere 285 (2021) 131480, https://doi.org/10.1016/j.chemosphere.2021.131480.
[72] E.F. Lessa, M.S. Gularte, E.S. Garcia, A.R. Fajardo, Orange waste: a valuable carbohydrate source for the development of beads with enhanced adsorption properties for cationic dyes, Carbohydr. Polym. 157 (2017) 660–668, https://doi.org/10.1016/j.carbpol.2016.10.019.
[73] M.G. Vaz, A.G.B. Pereira, A.R. Fajardo, A.C.N. Azevedo, F.H.A. Rodrigues, Methylene blue adsorption on chitosan-g-poly(acrylic acid)/Rice husk ash superabsorbent composite: kinetics, equilibrium, and thermodynamics, Water Air Soil Pollut. 228 (2017) 14, https://doi.org/10.1007/s11270-016-3185-4.
[74] J. Sun, Y. Wang, Y. He, J. Liu, L. Xu, Z. Zeng, Y. Song, J. Qiu, Z. Huang, L. Cui, Effective removal of nanoplastics from water by cellulose/MgAl layered double hydroxides composite beads, Carbohydr. Polym. 298 (2022) 120059, https://doi.org/10.1016/j.carbpol.2022.120059.
[75] H. Gomaa, E.M. Abd El-Monaem, A.S. Eltaweil, A.M. Omer, Efficient removal of noxious methylene blue and crystal violet dyes at neutral conditions by reusable montmorillonite/$NiFe_2O_4$@amine-functionalized chitosan composite, Sci.Rep. 12 (2022) 15499, https://doi.org/10.1038/s41598-022-19570-1.
[76] A. Hu, L. Liqing, M. Zhang, Y. Liu, G. Liao, D. Wang, Synthesis of highly water-dispersible adsorbent derived from alkali-modified hyper-cross-linked polymer for efficient removal of various organic contaminants and ammonia, J.Water Process Eng. 40 (2021) 101902, https://doi.org/10.1016/j.jwpe.2020.101902.
[77] H. Yang, Q. Feng, Characterization of pore-expanded amino-functionalized mesoporous silicas directly synthesized with dimethyldecylamine and its application for decolorization of sulphonated azo dyes, J. Hazard. Mater. 180 (2010) 106–114, https://doi.org/10.1016/j.jhazmat.2010.03.116.
[78] E. Alver, A.Ü. Metin, Anionic dye removal from aqueous solutions using modified zeolite: adsorption kinetics and isotherm studies, Chem. Eng.J. 200–202 (2012) 59–67, https://doi.org/10.1016/j.cej.2012.06.038.
[79] E.A. Mohamed, A.Q. Selim, S.A. Ahmed, L. Sellaoui, A. Bonilla-Petriciolet, A. Erto, Z. Li, Yanhui Li g, Moaaz K. Seliem, H_2O_2-activated anthracite impregnated with chitosan as a novel composite for Cr(VI) and methyl orange adsorption in single-compound and binary systems: modeling and mechanism interpretation, Chem. Eng. J. 380 (2020) 122445, https://doi.org/10.1016/j.cej.2019.122445.
[80] H. Xue, X. Wang, Q. Xu, F. Dhaouadi, L. Sellaou, M.K. Seliem, A.B. Lamine, H. Belmabrouk, A. Bajahzar, A. Bonilla-Petriciolet, Z. Li, Q. Li, Adsorption of methylene blue from aqueous solution on activated carbons and composite prepared from an agricultural waste biomass: a comparative study by experimental and advanced modeling analysis, Chem. Eng. J. 430 (2022) 13280, https://doi.org/10.1016/j.cej.2021.132801.
[81] R. Zhang, T. Leiviskä, Surface modification of pine bark with quaternary ammonium groups and its use for vanadium removal, Chem. Eng. J. 385 (2020) 123967, https://doi.org/10.1016/j.cej.2019.123967.
[82] I.K. Basha, E.M. Abd El-Monaem, R.E. Khalifa, A.M. Omer, A.S. Eltaweil, Sulfonated graphene oxide impregnated cellulose acetate floated beads for adsorption of methylene blue dye: optimization using response surface methodology, Sci. Rep. 12 (2022) 9339, https://doi.org/10.1038/s41598-022-13105-4.
[83] R. Foroutan, S.J. Peighambardoust, S. Ghojavand, M. Foroughi, A. Ahmadi, F. Bahador, B. Ramavandi, Development of a magnetic orange seed/Fe_3O_4 composite for the removal of methylene blue and crystal violet from aqueous media, Biomass Convers. Biorefinery 14 (2024) 25685–25700, https://doi.org/10.1007/s13399-023-04692-x.
[84] R.D. Hingrajiya, M.P. Patel, Fe_3O_4 modified chitosan based co-polymeric magnetic composite hydrogel: synthesis, characterization and evaluation for the removal of methylene blue from aqueous solutions, Int. J. Biol. Macromol. 244 (2023) 125251, https://doi.org/10.1016/j.ijbiomac.2023.125251.
[85] T. Benhalima, H. Ferfera-Harrar, N. Saha, Fe_3O_4 imbuing carboxymethyl cellulose/dextran sulfate nanocomposite hydrogel beads: an effective adsorbent for methylene blue dye pollutant. J. Macromol. Sci., part a, Pure Appl. Chem. 60 (6) (2023), https://doi.org/10.1080/10601325.2023.2212731.
[86] X. Sun, S. Yin, L. Zhao, W. Yang, Y. You, Adsorption properties of methylene blue and cu(II) on magnetically oxidized tannic acid cross-linked carboxymethyl chitosan gels, Int. J. Biol. Macromol. 278 (2024) 134709, https://doi.org/10.1016/j.ijbiomac.2024.134709.
[87] S. Heydari, S.E. Ahmadi, Fabrication and characterization of polymer based magnetic dialdehyde carboxymethyl cellulose/cysteine nanocomposites for methylene blue removal, Polym. Bull. 80 (2023) 3857–3882, https://doi.org/10.1007/s00289-022-04210-5.
[88] N. Faaizatunnisa, R. Ediati, H. Fansuri, H. Juwono, S. Suprapto, A.R.P. Hidayat, L. L. Zulfa, Facile green synthesis of core–shell magnetic MOF composites (Fe_3O_4@SiO_2@HKUST-1) for enhanced adsorption capacity of methylene blue, Nano-Struct. Nano-Objects. 34 (2023) 100968, https://doi.org/10.1016/j.nanoso.2023.100968.
[89] S. Hegazy, N.A. Abdelwahab, A.M. Ramadan, S.K. Mohamed, Magnetic Fe_3O_4-grafted cellulose/graphene oxide nanocomposite for methylene blue removal from aqueous solutions: synthesis and characterization, Next Mater. 3 (2023) 100064, https://doi.org/10.1016/j.nxmate.2023.100064.
[90] H. Ali, A.M. Ismail, Fabrication of magnetic Fe_3O_4/Polypyrrole/carbon black nanocomposite for effective uptake of Congo red and methylene blue dye: adsorption investigation and mechanism, J. Polym. Environ. 31 (2023) 976–998, https://doi.org/10.1007/s10924-022-02663-3.
[91] J. Zhang, H. Man, X. Han, Z. Wang, Y. Jiang, Facile preparation of magnetic P (MMA-co-GMA)@Fe_3O_4@PMAA microspheres using porous microsphere as templates for removal of methylene blue, Colloid Polym. Sci. 301 (2023) 933–947, https://doi.org/10.1007/s00396-023-05099-w.
[92] C. Wang, B. Zhang, X. Sun, Y. Zhang, W. Li, T. Yang, Y. Ma, Z. Sun, T. Li, Fabrication of core–shell Fe_3O_4@polypyrrole@sodium dodecyl benzene sulfonate composite for high-performance adsorption of methylene blue and malachite green in water, Sep. Purif. Technol. 329 (2024) 125140, https://doi.org/10.1016/j.seppur.2023.125140.
[93] M.A. Ludeña, F.L. Meza, R.I. Huamán, A.M. Lechuga, A.C. Valderrama, Preparation and characterization of Fe_3O_4/poly(HEMA-co-IA) magnetic hydrogels for removal of methylene blue from aqueous solution, Gels 10 (1) (2024) 15, https://doi.org/10.3390/gels10010015.
[94] A. Banaei, A. Saadat, R. Javadi, Preparation magnetic graphene oxide/diethylenetriamine composite for removal of methylene blue from aqueous solutions, Sci. Rep. 14 (2024) 15457, https://doi.org/10.1038/s41598-024-65628-7.
[95] D.D.A. Buelvas, L.P. Camargo, I.K.I. Salgado, B.L.S. Vicentin, D.F. Valezi, L. H. Dall'Antonia, C.R.T. Tarley, E.D. Mauro, Study and optimization of the adsorption process of methylene blue dye in reusable polyaniline-magnetite composites, Synth. Met. 292 (2023) 117232, https://doi.org/10.1016/j.synthmet.2022.117232.
[96] A. Akbari, H. Abbasi, M. Shafiee, H. Baniasadi, Synergistic adsorption of methylene blue with carrageenan/hydrochar-derived activated carbon hydrogel composites: insights and optimization strategies, Int. J. Biol. Macromol. 265 (2024) 130750, https://doi.org/10.1016/j.ijbiomac.2024.130750.
[97] R. Rahmi, L. Lelifajri, F. Fathurrahmi, H. Fathana, M. Iqhrammullah, Preparation and characterization of PEGDE-EDTA-modified magnetic chitosan microsphere as an eco-friendly adsorbent for methylene blue removal, S. Afr. J. Chem. Eng. 43 (2023) 296–302, https://doi.org/10.1016/j.sajce.2022.11.009.
[98] V.S. Munagapati, H.-Y. Wen, A.R.K. Gollakota, J.-C. Wen, K.-Y.A. Lin, C.-M. Shu, V. Yarramuthi, P.K. Basivi, G.M. Reddy, G.V. Zyryanov, Magnetic Fe_3O_4 nanoparticles loaded guava leaves powder impregnated into calcium alginate hydrogel beads (Fe_3O_4-GLP@CAB) for efficient removal of methylene blue dye from aqueous environment: synthesis, characterization, and its adsorption performance, Int. J. Biol. Macromol. 246 (2023) 125675, https://doi.org/10.1016/j.ijbiomac.2023.125675.
[99] I.H. Alsohaimi, M.S. Alhumaimess, A.A. Alqadami, H.M.A. Hassan, Q. Chen, M. S. Alamri, M.M.J. Alanzi, T.S. Alraddadi, Chitosan-carboxylic acid grafted multifunctional magnetic nanocomposite as a novel adsorbent for effective removal of methylene blue dye from aqueous environment, Chem. Eng. Sci. 280 (2023) 119017, https://doi.org/10.1016/j.ces.2023.119017.
[100] M. Jourbonyan, M. Safarnia, F. Raji, A.D. Koohi, Magnetic sodium alginate/hydroxyapatite nanocomposite as an efficient biosorbent for rapid adsorption of methylene blue, Korean J. Chem. Eng. 40 (2023) 124–135, https://doi.org/10.1007/s11814-022-1203-3.

[101] K.M. Rehan, K.A. Basha, S.M. Safiullah, Synthesis of poly(Glycidyl methacrylate) based hybrid materials and evaluation of methylene blue adsorption: structural characterization and adsorption behaviour, J. Inorg. Organomet. Polym. Mater. 33 (2023) 2172–2187, https://doi.org/10.1007/s10904-023-02671-3.
[102] P. Kumari, M.K. Nayak, D. Dhruwe, M.K. Patel, S. Mishra, Synthesis and characterization of sulfonated magnetic graphene-based cation exchangers for the removal of methylene blue from aqueous solutions, Ind. Eng. Chem. Res. 62 (2023) 1245–1256, https://doi.org/10.1021/acs.iecr.2c04432.
[103] I.H. Alsohaimi, M.S. Alhumaimess, A.A. Alqadami, G.T. Alshammari, R.F. Al-Olaimi, A.A. Abdeltawab, M.Y. El-Sayed, H.M. Hassan, Adsorptive performance of aminonaphthalenesulfonic acid modified magnetic-graphene oxide for methylene blue dye: mechanism, isotherm and thermodynamic studies, J. Inorg. Organomet. Polym. Mater. 147 (2023) 110261, https://doi.org/10.1016/j.inoche.2022.110261.
[104] M.S. Kafshgari, M. Jahanshahi, M. Ghorbani, Magnetic coordination polymer for dye removal and antibacterial activity, J. Taiwan Inst. Chem. Eng. 149 (2023) 104995, https://doi.org/10.1016/j.jtice.2023.104995.
[105] N.O. Rubangakene, M. Elkady, A. Elwardany, M. Fujii, H. Sekiguchi, H. Shokry, Effective decontamination of methylene blue from aqueous solutions using novel nano-magnetic biochar from green pea peels, Environ. Res. 220 (2023) 115272, https://doi.org/10.1016/j.envres.2023.115272.
[106] S.J. Peighambardoust, F.K. Halimi, P.M. Pakdel, H. Safarzadeh, Decontamination of methylene blue from aqueous media using alginate-bonded polyacrylamide/carbon black nanocomposite hydrogel, Polym. Adv. Technol. 35 (2024) e6336, https://doi.org/10.1002/pat.6336.
[107] K.S. Lau, N.A.S. Azmi, S.X. Chin, S. Zakaria, C.H. Chia, Chitosan-bead-encapsulated polystyrene sulfonate for adsorption of methylene blue and regeneration studies: batch and continuous approaches, Polymers 15 (2023) 1269, https://doi.org/10.3390/polym15051269.
[108] P. Ilgin, A. Onder, M.R. Kıvanç, H. Ozay, O. Ozay, Adsorption of methylene blue from aqueous solution using poly(2-Acrylamido-2-Methyl-1-Propanesulfonic acid-co-2-hydroxyethyl methacrylate) hydrogel crosslinked by activated carbon, J. Macromol. Sci. Part A. 60 (2023) 135–149, https://doi.org/10.1080/10601325.2023.2165945.
[109] Y.X. Ma, W.J. Shao, W. Sun, Y.L. Kou, X. Li, H.P. Yang, One-step fabrication of β-cyclodextrin modified magnetic graphene oxide nanohybrids for adsorption of Pb (II), cu (II) and methylene blue in aqueous solutions, Appl. Surf. Sci. 459 (2018) 544–553, https://doi.org/10.1016/j.apsusc.2018.08.025.
[110] T.A. Khan, S. Dahiya, I. Ali, Use of kaolinite as adsorbent: equilibrium, dynamics and thermodynamic studies on the adsorption of rhodamine B from aqueous solution, Appl. Clay Sci. 69 (2012) 58–66, https://doi.org/10.1016/j.clay.2012.09.001.
[111] M.C. Manoko, E.M.M. Chirwa, K. Makgopa, Non-demineralized paper waste sludge derived magnetic biochar as sorbs for removal of methylene blue, phosphorus, and selenate in wastewater, Clean. Chem. Eng. 3 (2022) 100048, https://doi.org/10.1016/j.clce.2022.100048.
[112] I. Anastopoulos, M.J. Ahmed, E.H. Hummadi, Eucalyptus-based materials as adsorbents for heavy metals and dyes removal from (waste)waters, J. Mol. Liq. 356 (2022) 118864, https://doi.org/10.1016/j.molliq.2022.118864.
[113] S. Tripathy, S. Sahu, R.K. Patel, R.B. Panda, P.K. Kar, Novel Fe_3O_4-modified biochar derived from citrus Bergamia peel: a green synthesis approach for adsorptive removal of methylene blue, ChemistrySelect 7 (2022) e202103595, https://doi.org/10.1002/slct.202103595.
[114] Q.-Q. Zhou, L. Qiu, M.-Q. Zhu, *Eucommia ulmoides* Oliver derived magnetic activated carbon for eliminating methylene blue from dyeing wastewater and its economic efficiency assessment, Ind. Crop. Prod. 187 (2022) 115537, https://doi.org/10.1016/j.indcrop.2022.115537.